processes

MDPI

Article

A Strategy for Suppressing Novel Harmonics of Distributed Photovoltaics in Distribution Networks Based on APF–LCLLC

Feng Zhou [1,*], Shuhang Zhang [1], Shun Li [2], Yukun Su [3], Chao Yang [4], Shengqi Zhou [4] and Jingui Lv [5]

[1] College of Electrical Engineering and Automation, Shandong University of Science and Technology, Qingdao 266590, China
[2] State Grid Shandong Electric Power Company Qingdao Huangdao District Power Supply Company, Qingdao 266400, China
[3] State Grid Shandong Province Electric Power Corporation Xintai Power Supply Company, Taian 271200, China
[4] State Grid Shandong Electric Power Company Qingdao Power Supply Company, Qingdao 266000, China
[5] Qingdao Hisense Hitachi Air-Conditioning Systems Co., Ltd., Qingdao 266510, China
* Correspondence: zhoufeng@sdust.edu.cn

Abstract

In distribution networks with a high proportion of renewable energy and a high proportion of power electronics (High-RE-PE), harmonics generated by distributed photovoltaic (PV) systems and nonlinear loads coexist at multiple frequencies. Assessing the compensation performance of hybrid filtering strategies can inform the design of mitigation schemes for novel harmonics in distribution networks. Harmonic mitigation requires coordination between selective compensation of characteristic harmonics and attenuation of higher-frequency harmonics. An active power filter (APF) and an LCLLC passive filter are connected in series to form a hybrid branch in parallel with the load. The LCLLC filter attenuates higher-frequency harmonics, while the APF uses combined proportional–integral (PI) and quasi-proportional resonant (quasi-PR) control based on complementary decomposition of the tracking error. Quasi-PR regulates the error for the target characteristic harmonics, while PI regulates the residual error. Line and distribution transformer loss models are used to calculate equipment losses for different harmonic spectra. Compensation performance is compared across controller parameter settings. A MATLAB/Simulink model incorporating distributed PV generation and nonlinear loads is developed to verify system-level compensation performance. In the simulated case, APF–LCLLC compensation reduces the total harmonic distortion (THD) of the system current to 1.53%, considerably below 3.74% with APF compensation alone. The current waveform and harmonic spectrum are further improved. These results demonstrate effective compensation by the hybrid filtering structure in the examined case involving multiple harmonic sources. They offer a new approach to mitigating novel harmonics in distribution networks with distributed PV.

Keywords: a high proportion of renewable energy and a high proportion of power electronics; distributed photovoltaic; novel harmonics; line loss; APF–LCLLC

Check for updates

Academic Editor: Massimo Caruso

Received: 20 October 2026
Revised: 16 November 2026
Accepted: 20 November 2026
Published: 26 November 2026

Copyright: © 2026 by the authors. Licensee MDPI, Basel, Switzerland. This article is an open access article distributed under the terms and conditions of the Creative Commons Attribution (CC BY) license.

1. Introduction

Electricity demand continues to increase, pressure to protect the environment intensifies, and power electronics technology continues to advance. In this context, renewable energy sources, particularly distributed photovoltaic (PV) generation, and their associated power electronic equipment have been widely deployed. High-RE-PE power systems are characterized by a high proportion of renewable energy and a high proportion of power

electronics. In these systems, novel harmonics generated by the large-scale integration of distributed PV systems pose challenges to the safe and stable operation of distribution networks. The spatially dispersed and time-varying nature of these harmonic sources can intensify harmonic fluctuations [1] and may degrade power quality and increase electrical equipment losses [2].

As the proportion of power electronic equipment increases, harmonics generated by inverter nonidealities may be superimposed. Dead-time effects primarily introduce low-order harmonics, whereas sinusoidal pulse-width modulation (SPWM) generates high-frequency harmonics near the switching frequency. Together, these components result in wideband harmonic pollution [3]. The characteristics of novel harmonics are also affected by their generation mechanisms, modulation delays, and dynamic interactions between inverters and the grid [4]. Harmonic currents injected into the distribution network produce voltage drops across the system impedance, resulting in voltage distortion at the point of common coupling (PCC). These harmonics may also couple with disturbances such as wideband oscillations and voltage fluctuations [5]. In addition, adverse impedance interactions between inverters and the distribution network may reduce system damping, promote sustained harmonic amplification, and trigger harmonic instability. This instability may distort the inverter-side AC bus voltage [6]. The resulting positive feedback loop may interfere with the normal operation of renewable power systems. Mitigating novel harmonics in distribution networks therefore presents systemic challenges.

Research on harmonic generation mechanisms, measurement methods, and system-level impacts has advanced alongside the development of renewable energy and power electronic equipment. Han et al. [7] modeled and simulated a microgrid based on harmonic generation mechanisms and analyzed harmonic components generated when nonlinear loads were switched on and off. Zhe et al. [8] investigated typical harmonic-source models in modern power systems. Their work provided a basis for understanding harmonic distortion mechanisms and developing mitigation strategies. Xu et al. [9] investigated secondary-sideband harmonic emissions from grid-connected inverters operating individually and in parallel. The study addressed complex harmonic behavior associated with parallel converters and background harmonics in emerging power systems. The results showed that harmonic pollution may increase because of frequency coupling between background and converter harmonics, as well as harmonic interactions among parallel converters. These effects may also complicate harmonic mitigation in distribution networks. Li et al. [10] further showed that coupling multiple grid-connected inverters with grid impedance forms a high-order impedance network. Background harmonic disturbances may excite multimode wideband resonance in this network. Such resonance may adversely affect the safe and stable operation of distribution networks.

As PV penetration increases and grid-connected PV deployment expands, research has addressed grid-connected inverter topologies, control strategies, and operational issues in grid-connected PV systems [11]. Based on measured harmonic data, Yuan et al. [3] proposed a method for calculating harmonic losses in low-voltage distribution networks. Harmonic losses accounted for approximately 0.6% of total network losses in the distribution network studied. Although this proportion was small, the additional losses caused by harmonics still warrant attention because total losses in large-scale low-voltage distribution networks are substantial. Karimi et al. [12] systematically reviewed the effects of PV integration on voltage fluctuations, voltage unbalance, harmonics, and islanding in distribution networks. They summarized operational issues associated with increasing PV penetration.

From a system-planning perspective, Erenoğlu et al. used measured harmonic data from household nonlinear loads to construct a load power profile and compared the capacity-sizing results for a grid-connected PV–energy storage system obtained using this profile and

a rated-power profile [13], thereby incorporating harmonic information into capacity-sizing analysis. In terms of grid-connected operation, E. Zhao et al. [14] used an impedance-based model to analyze harmonic amplification in grid-connected PV systems under weak-grid conditions and proposed a harmonic suppression strategy combining multi-resonant current control and active damping. Z. Shao et al. [15] reviewed methods for harmonic analysis and suppression in power grids with renewable energy integration, focusing on harmonic-source modeling and harmonic-interaction mechanisms. Taken together, the studies discussed above address harmonic losses, system planning, harmonic interactions, and suppression strategies, providing a foundation for harmonic analysis and mitigation in distribution networks with PV integration.

Passive filters have traditionally been one of the main means of suppressing harmonic distortion in power systems. Their cost, losses, harmonic suppression performance, and reactive power compensation capability depend on parameter design. Trade-offs also exist among these design objectives [16]. Existing studies therefore generally formulate passive filter parameter design as single- or multi-objective optimization problems. Objectives include minimizing filter cost or losses, minimizing current or voltage harmonic distortion, and maximizing the power factor [17]. Zhao et al. [18] optimized LCLLC filter parameters using an improved multi-objective particle swarm optimization algorithm. Their simulations showed that the total harmonic distortion (THD) of the grid current could be reduced to 0.55%. Jia et al. [19] proposed a composite control strategy to address resonance and harmonic currents in LCL-filtered grid-connected inverters operating in weak grids. The strategy combines resonant feedforward, active damping, quasi-proportional resonant (quasi-PR) control, and harmonic compensation. This combination improves grid current quality. The scope of this research has expanded from component parameter design to control strategy optimization. However, filter parameter selection and controller tuning remain the main focus. Cheepati et al. [20] proposed a parametric design method for a triple-tuned passive filter. A single filter branch suppresses three dominant harmonic orders simultaneously and improves filtering performance for both static and dynamic loads. The method offers a design approach that considers both multiple-harmonic suppression and filter cost-effectiveness.

Compared with passive filters, an active power filter (APF) can inject compensating currents in response to changes in harmonics, providing greater dynamic compensation capability [21]. Among APF configurations, the shunt active power filter (SAPF) is commonly used for harmonic current compensation. In addition to filter topology, current control strategies also influence the compensation performance of active and hybrid filters. To address uncertainties in system models and external disturbances, Ding et al. [22] combined neural-network-based estimation of unknown system dynamics with sliding-mode control, reducing the controller's dependence on an accurate mathematical model and improving harmonic suppression performance. Daou et al. [23] combined backstepping control and second-order sliding-mode control within a direct power control framework, reporting post-compensation grid-side current THD values of 0.91% in simulation and 3.17% in experiments. Different control methods have distinct characteristics in terms of dynamic response, steady-state compensation accuracy, and implementation complexity, and their selection should take into account the specific filter topology and compensation requirements [24].

Previous studies have proposed various filter topologies and control strategies for harmonic mitigation in distributed PV systems [25,26]. For a thyristor-controlled LC-coupling hybrid active power filter (TCLC-HAPF), Sou et al. [27] employed a multi-quasi-proportional-resonant (MQPR) controller with resonant-gain scheduling to accommodate inductive and capacitive loads. When multiple harmonic orders coexist in High-RE-PE

distribution networks, an aggregate distortion metric alone cannot adequately reflect differences in equipment response arising from harmonic spectral composition. Likewise, a single steady-state metric is insufficient to characterize the trade-offs among harmonic suppression, compensating-current requirements, and dynamic recovery. Therefore, the evaluation of harmonic mitigation schemes should consider both the effects of harmonic spectra on equipment and the performance trade-offs during compensation.

To address the need for multi-frequency harmonic mitigation in High-RE-PE distribution networks with both distributed photovoltaic (PV) generation and nonlinear loads, this study investigates an APF–LCLLC hybrid filtering strategy and analyzes equipment response and compensation performance. Loss models for lines and distribution transformers are used to compare equipment metrics across selected characteristic-harmonic spectra with the same aggregate THD and to examine trade-offs in allocating compensation among different harmonic orders under a fixed compensation budget. Compared with hybrid filter designs emphasizing resonant-branch configuration and gain tuning, the proposed strategy combines the LCLLC network's attenuation of higher-frequency harmonics with a complementary decomposition of the APF current-loop tracking error. The APF is connected to the point of common coupling (PCC) through the passive LCLLC filter, and the hybrid filter as a whole is connected in parallel with the load. In the APF current loop, the quasi-proportional-resonant (quasi-PR) controller regulates the error components associated with the selected 5th, 7th, 11th, and 13th harmonics, while the proportional–integral (PI) controller regulates the remaining tracking error. Controller-parameter comparisons are used to assess residual harmonics, compensating-current requirements, and recovery performance following harmonic-spectrum switching. The effectiveness of APF–LCLLC compensation is further verified in a system with distributed PV and nonlinear loads, using uncompensated and APF-only compensation cases as references.

2. Analysis of the Novel Harmonic Characteristics of Distributed Photovoltaics

2.1. Structure of Distributed Photovoltaic Power Generation System

The single-diode equivalent circuit shown in Figure 1 is used as the basis for modeling the PV source, with the series resistance R_s accounting for the internal resistive voltage drop and the shunt resistance R_{sh} accounting for leakage current through the parallel path. Previous studies have shown that single-diode and two-diode models involve trade-offs among the accuracy of PV I–V characteristic representation, parameter complexity, and computational cost [28]. In addition, the parameters of the single-diode model can be estimated from key specifications provided in PV module datasheets under standard test conditions [29]. In this study, the PV array is connected to the distribution network through a Boost converter and a grid-connected inverter, and the PV model is primarily used to describe the PV array's I–V output characteristics under variations in temperature and irradiance and to provide the DC-side input. Since this study focuses on system harmonics and their mitigation in the presence of distributed PV generation and nonlinear loads, rather than on detailed modeling of the internal physical processes of PV cells, a simplified engineering model based on the single-diode equivalent circuit is adopted. The equivalent circuit of the PV cell is shown in Figure 1.

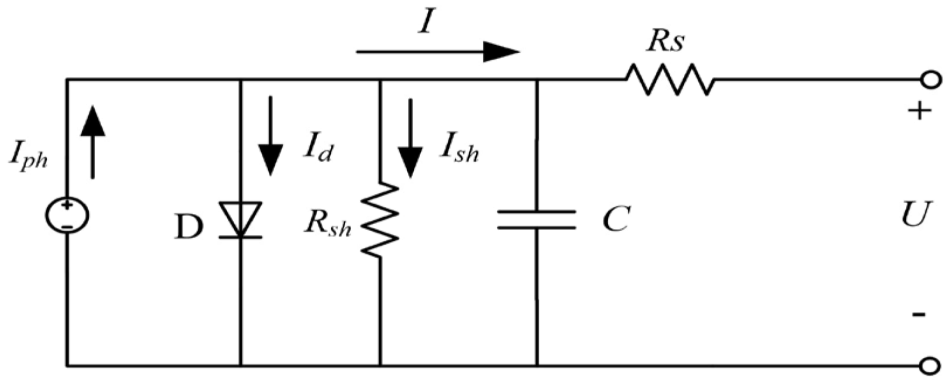

Figure 1. Equivalent circuit of photovoltaic cell.

Based on the equivalent-circuit relations and the current–voltage characteristic of the PN junction, the output current of the photovoltaic cell can be expressed as follows [30]:

$$\begin{aligned} I &= I_{ph} - I_0(\exp(q(U + IR_S)/ART) - 1) \\ &\quad -(U + IR_s)/R_{sh} \end{aligned} \tag{1}$$

where I: indicates PV cell output current; U: indicates PV cell output voltage; I_{ph}: indicates photogenerated current; I_0: indicates diode reverse saturation current; q: indicates electron charge, 1.6×10^{-19} C; Rs: indicates series resistance; R_{sh}: indicates parallel resistance; K: indicates Boltzmann constant, 1.38×10^{-23} J/K; T: indicates absolute temperature; To describe the steady-state current–voltage characteristics on the source side, the model uses the diffusion-current approximation for an ideal PN junction at low injection levels. Depletion-region recombination current is neglected, and A is set to 1.

To develop an engineering model of the PV source based on reference module parameters, the shunt leakage-current term $\frac{U+IR_s}{R_{sh}}$ is neglected, the voltage drop across the series resistance is approximated, and $I_{ph} \approx I_{sc}$ is assumed. The resulting expression is:

$$I = I_{sc}[1 - B(\exp(U/(CU_{oc})) - 1)] \tag{2}$$

By applying the open-circuit and maximum power point conditions to Equation (2), the model coefficients B and C can be determined under the corresponding exponential approximation:

$$C = (U_m/U_{oc} - 1)[\ln(1 - I_m/I_{sc})]^{-1} \tag{3}$$

In practical engineering applications, photovoltaic cells are affected by changes in their surrounding environment. Among these factors, ambient temperature and irradiance are the main parameters influencing the current-voltage characteristic curve of PV cells. Therefore, a correction method must be adopted to compensate for the errors caused by parameter discrepancies between standard operating conditions and actual operating conditions. The correction method selected in this paper is as follows [31]:

$$\Delta t = t - t_{ref} \tag{4}$$

$$\Delta s = s/s_{ref} - 1 \tag{5}$$

$$I'_{sc} = I_{sc}\left(s/s_{ref}\right)(1 + a\Delta t) \tag{6}$$

$$U'_{oc} = U_{oc}(1 - c\Delta t)\ln(e + b\Delta s) \tag{7}$$

$$I'_m = I_m\left(s/s_{ref}\right)(1 + a\Delta t) \tag{8}$$

$$U'_m = U_m(1 - c\Delta t)\ln(e + b\Delta s) \tag{9}$$

where: t_{ref}: indicates the temperature under standard conditions; s_{ref}: indicates irradiance under standard conditions; a, b, and c are the correction factors for photovoltaic systems in temperate regions. The specific values of the parameters known in the formula are shown in Table 1.

Table 1. Set values of each parameter.

Parameter Name	Parameter Values
t_{ref}/°C	25
s_{ref}/W/m^2	1000
a	0.0025
b	0.5
c	0.00288

The values of I_m, I_{sc}, U_{oc}, and U_m in the final mathematical model are taken from the actual photovoltaic cell parameters. I_m, I_{sc}, U_{oc}, and U_m denote the standard test parameters of the photovoltaic cell under a reference temperature of 25 °C and an irradiance of 1000 W/m^2. This system enables the analysis of the PV cell's steady-state output characteristics by controlling temperature and irradiance. The parameters of the individual PV cell simulation model built in this system are shown in Table 2.

Table 2. Parameters of photovoltaic cells under standard test conditions.

Parameter Name	Parameter Values
Open-circuit voltage U_{oc}/V	36.3
Peak operating voltage U_m/V	29
Short-circuit current I_{sc}/A	7.84
Peak operating current I_m/A	7.35

The PV cell model was implemented in MATLAB/Simulink, and its functional block diagram is shown in Figure 2.

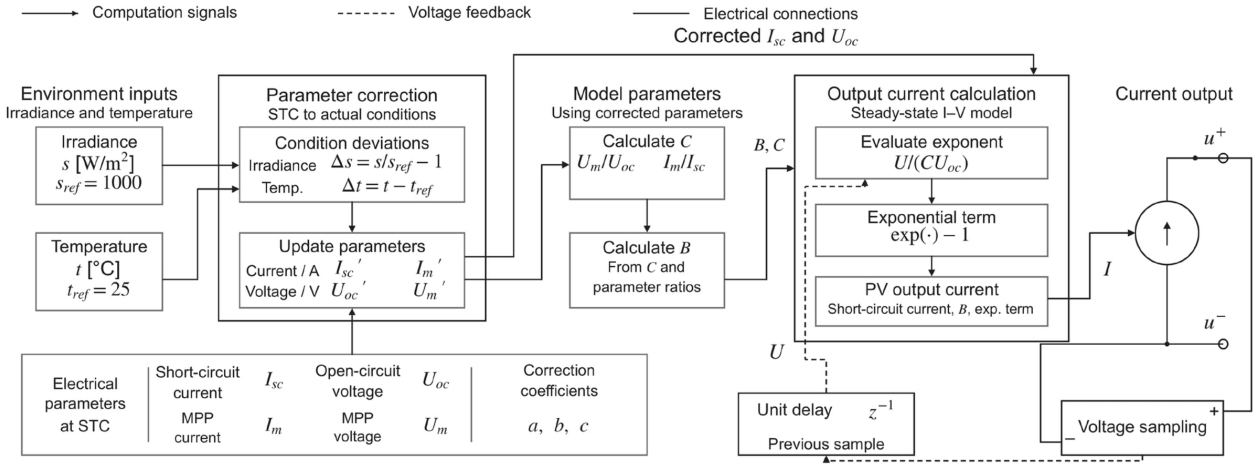

Figure 2. Photovoltaic cell simulation model.

The simulations examine the effects of irradiance variations at the standard temperature and temperature variations at the standard irradiance on the I–V and P–V characteristics of the PV cell. The results show that increasing irradiance primarily increases the short-circuit current and maximum output power, whereas increasing temperature primarily decreases the open-circuit voltage and maximum output power. The developed model incorporates

PV module reference parameters and temperature and irradiance corrections to characterize PV output under different environmental conditions and serves as the PV source model for subsequent grid-connected system simulations.

2.2. Analysis of the Characteristics of Novel Harmonics in Distributed PV Systems

2.2.1. Analysis of Harmonic Sources in PV Systems

Analysis of Novel Harmonic Characteristics in Distribution Networks with Distributed PV

DC power from a PV array is converted into AC power by a grid-connected inverter and then fed into the distribution network. Nonlinear loads and inverter nonidealities may introduce low- and medium-order harmonics. Inverter control and interactions between the inverter and the grid also affect harmonic characteristics. High-frequency switching of power electronic devices within the inverter also generates high-frequency components associated with the switching frequency and its multiples. Therefore, harmonics at the grid connection point in a distribution network with distributed PV originate from multiple sources and are characterized by a wide frequency distribution. The propagation of these frequency components through the network is also affected by filtering stages and network impedance. This section analyzes harmonic characteristics at the grid connection point from three perspectives: variations in operating conditions, harmonic frequency distribution, and the coexistence of multiple sources. It also discusses the corresponding mitigation requirements.

(a) Harmonic Analysis of PV Sources

Harmonic Characteristics with Varying Operating Conditions

Compared with a single PV cell, the output characteristics of a PV array are jointly affected by irradiance, ambient temperature, and the operating states of its modules. Irradiance variations primarily affect the array's output current and power, whereas temperature variations primarily affect its output voltage and power characteristics. When irradiance is nonuniform, individual modules receive different irradiance levels, and the array's DC-side voltage, current, and output power exhibit more complex fluctuations. The PV array itself produces DC power, and changes in its operating state do not directly generate AC-side harmonics. Changes in irradiance and temperature, as well as nonuniform irradiance, cause variations in the DC-side output. These variations alter the input conditions and operating points of downstream power conversion stages and affect the harmonic characteristics of the grid-connected output. At low irradiance, the PV array's output power and the fundamental component of the grid current decrease. In these conditions, the relative contribution of harmonic components increases, resulting in a higher grid current THD. Therefore, the influence of the PV source on grid-connected harmonics clearly depends on operating conditions.

(b) Harmonic Analysis of Energy Conversion Components

Harmonic Frequency Distribution and Frequency Bands for Mitigation

In a PV system with a two-stage power conversion structure, the first stage uses a Boost DC/DC converter to step up the DC voltage. Maximum Power Point Tracking (MPPT) in the first stage is implemented using the incremental conductance method. The second stage uses a three-phase bridge inverter for DC/AC conversion. Periodic switching of the inverter's power switches introduces corresponding harmonic components into the inverter

output voltage in addition to the fundamental component. The output line-to-line voltage of the three-phase bridge inverter is expressed in [32] as:

$$U_{AB} = \frac{2\sqrt{3}}{\pi} U_d \sum_{n=1,3,5\cdots}^{\infty} \frac{1}{n} \sin(n\omega t + \lambda) \tag{10}$$

IGBTs have finite turn-on and turn-off times, so a dead-time interval is required between the gate-drive signals of the upper and lower switches in the same inverter leg. This interval is used to prevent shoot-through caused by simultaneous conduction of the two switches. Dead time alters the effective duration of ideal SPWM gate pulses, causing the inverter's actual output voltage to deviate from the ideal modulated voltage and introducing additional voltage harmonics. To account for dead-time effects, the expression for the output line-to-line voltage of the inverter can be modified as follows:

$$\begin{aligned} U_{Td} &= \frac{4}{\pi} N f T_d U_d \\ &\times \sum_{n=1}^{\infty} \frac{(-1)^{n+1}}{2n-1} \cos\left[(2n-1)\left(\omega t + \frac{\pi}{2} - \varphi\right)\right] \end{aligned} \tag{11}$$

Here, f denotes the switching frequency, and φ denotes the power factor angle.

With distributed PV connected to the grid, the grid current spectrum is jointly affected by operating states, harmonic sources, and circuit transfer characteristics. Operating conditions such as irradiance and ambient temperature affect the inverter's operating state by changing the DC-side operating point. Switching of power electronic devices generates frequency components other than the fundamental in the inverter output voltage. Filtering and grid-connection circuits affect how these components appear in the grid current. When other harmonic sources, such as nonlinear loads, are present, their harmonic injections also affect the spectrum at the grid connection point. Therefore, the grid current spectrum cannot be directly equated with the theoretical output spectrum of a single inverter. Theoretical characteristic harmonic orders indicate which orders may occur for a given set of conditions. The amplitudes of individual harmonics cannot be inferred from their orders alone. Individual harmonic content indicates the amplitude of each harmonic current relative to that of the fundamental current. Total Harmonic Distortion (THD) reflects the overall level of current distortion due to harmonics, but does not uniquely determine the amplitude distribution among harmonic orders. Therefore, the same THD value may correspond to different spectral compositions.

(c) Analysis of Harmonics Generated by Nonlinear Loads

Harmonic Characteristics at the Grid Connection Point with Multiple Coexisting Sources

Nonlinear loads in a PV system mainly consist of various power electronic components. AC sources provide AC power to users, whereas power electronic power supplies typically use rectifier circuits to convert AC into a DC voltage before supplying power. The DC-side voltage is expressed as:

$$U_d = U_{d0} + \sum U_{dk} \sin(k\omega t + \delta_k) \tag{12}$$

An explicit expression for the DC-side voltage is:

$$\begin{aligned} U_d(t) &= \frac{3\sqrt{6}}{\pi} \\ &+ \frac{3\sqrt{6}}{\pi} \sum_{n}^{\infty} (-1)^b \left[\frac{1}{n+1} - \frac{1}{n-1}\right] cosn\omega t \end{aligned} \tag{13}$$

The expression shows that the DC-side voltage of the rectifier load consists of a DC component and a periodic ripple component. For a six-pulse rectifier, the AC-side current

contains characteristic harmonics of orders $6k \pm 1$, whereas the DC-side voltage contains ripple components of orders 6k, reflecting the spectral characteristics of nonlinear conduction. When grid-connected distributed PV systems and nonlinear loads such as rectifiers operate in the same distribution network, their harmonics may exhibit different frequency compositions and phase characteristics. At the grid connection point, the resultant harmonic component of a given order is affected by the phase relationships among harmonic sources. Network impedance and the voltage at the grid connection point also affect this component. Consequently, harmonics of the same order may reinforce or partially cancel each other. Nonlinear loads are also an important source of harmonics in distribution networks. Therefore, harmonic analysis of grid-connected distributed PV systems should consider operating conditions, harmonic sources, propagation paths, and the response at the grid connection point.

2.2.2. Simulation and Analysis of Photovoltaic Power Generation System

Grid-connected PV is a photovoltaic (PV) power generation system that is connected to the power system. The DC energy of the PV power system is converted into AC energy of the same frequency as the grid by a converter. In this paper, the structural diagram shown in Figure 3 is used to study the problem of dynamic mathematical modeling of a grid-connected PV power plant.

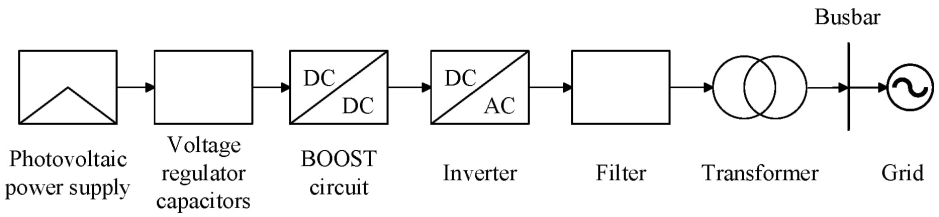

Figure 3. Photovoltaic grid-connected structure diagram.

In order to realize the same frequency and phase of current and voltage in the grid, this section adopts phase-locked loop technology, and the active and reactive currents of the PV grid-connected inverter can be controlled separately by the d and q axes; therefore, this paper adopts the PI controller under the synchronous rotating coordinate system to realize the control of voltage and current. Based on the PV cell system built above, this section builds a model of the PV power generation system in MATLAB as shown in Figure 4; its functional structure is shown in Figure 5.

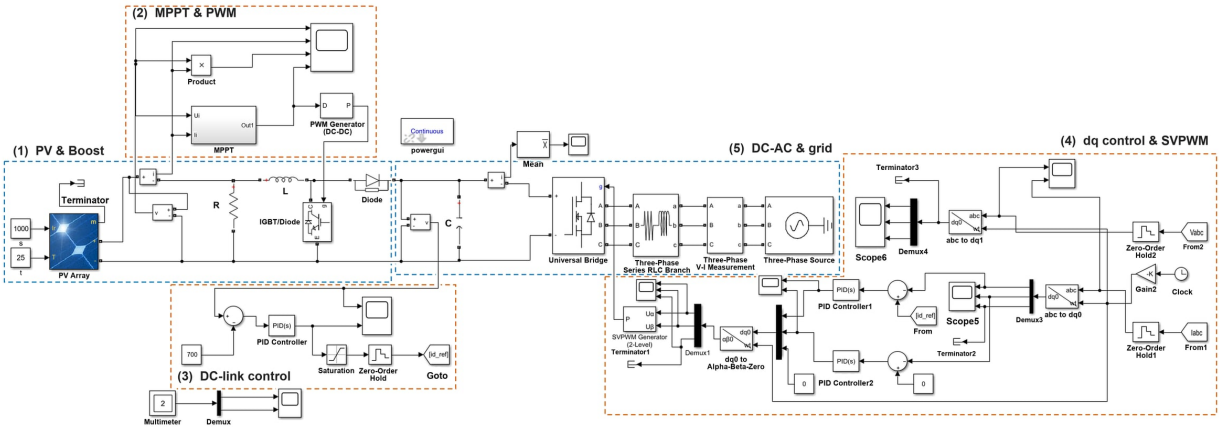

Figure 4. Photovoltaic power generation system simulation model diagram.

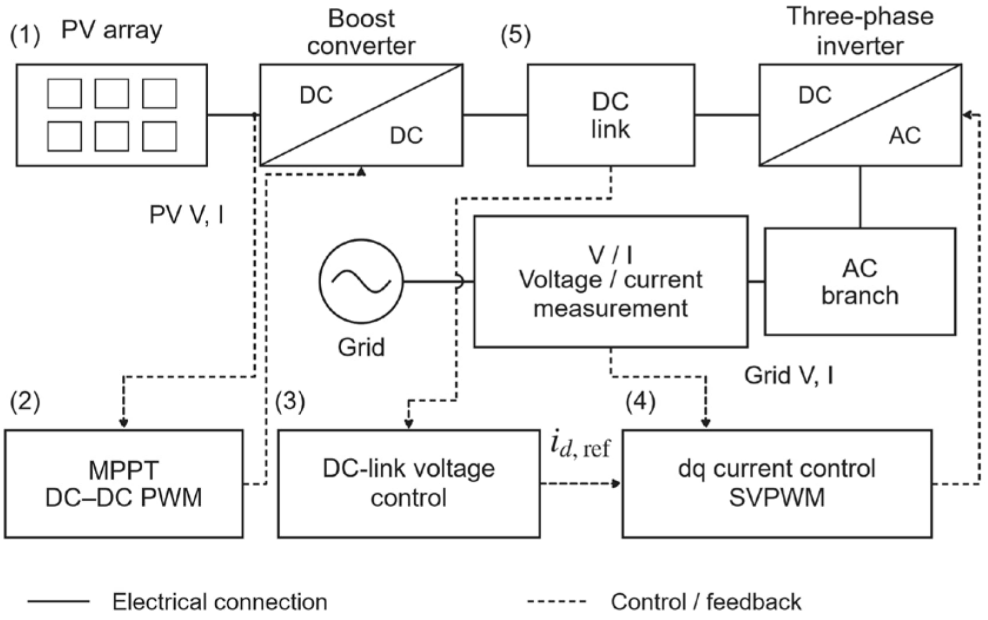

Figure 5. Functional structure of the photovoltaic power generation system.

In Figure 5, labels (1)–(5) denote the PV array, MPPT and DC–DC PWM control, DC-link voltage control, dq current control, and DC link, respectively. The symbol $i_{\mathrm{d,ref}}$ denotes the d-axis current reference. The simulation parameters of the PV power system are set as shown in Table 3.

Table 3. Photovoltaic power generation system simulation parameter setting.

Parameter Symbol	Parameter Value
DC Side Voltage/V	700
AC Side Voltage/V	380
Filter Side Inductor/H	2×10^{-2}
Boost Circuit Inductors/H	6×10^{-2}
Boost Circuit Capacitors/F	1
Boost Circuit Resistors/Ω	0.1
Simulation duration (s)	1
Numerical solver	ode23tb
Integration scheme	Variable-step
Electrical network simulation mode	Continuous
Maximum time step (μs)	1
Boost converter switching frequency (kHz)	5
PV inverter switching frequency (kHz)	1.5
Fundamental frequency (Hz)	50

The parameters of the Boost circuit are set as shown in Table 4.

Table 4. Circuit parameter setting.

Parameter Symbols	Parameter Values
L/H	6×10^{-2}
C/F	1
R/Ω	0.1

The simulation results are shown in Figure 6.

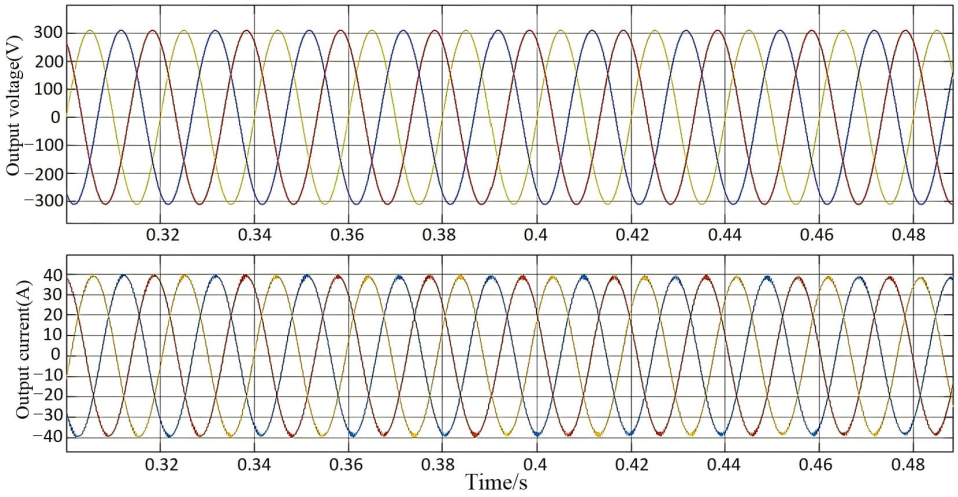

Figure 6. Photovoltaic power generation system simulation output waveform.

Figure 6 shows the three-phase voltage and current of the PV power generation system after it is connected to the distribution network. As can be seen from Figure 7, the current total harmonic distortion (THD) after grid connection is 8.46%, which does not meet the grid connection requirement of 5% THD. The output current harmonics of the photovoltaic power generation system contain more harmonic parameters as shown in Table 5.

As can be seen from Table 5, the harmonic components of the output current of the PV power generation system are mainly the 5th, 7th, 11th, 13th and other 6k ± 1 harmonic components, and the harmonic content is influenced by the filtering effect, which is consistent with the above theoretical analysis of the harmonic characteristics of the PV power generation system. Moreover, its harmonic components are not only low harmonics but also have a high content of higher harmonics near the switching frequency. Therefore, with the rapid development of renewable energy, the total amount of distributed new energy in the power system is getting larger and larger, which will inevitably have a serious impact on the power supply quality and stable operation of the power system.

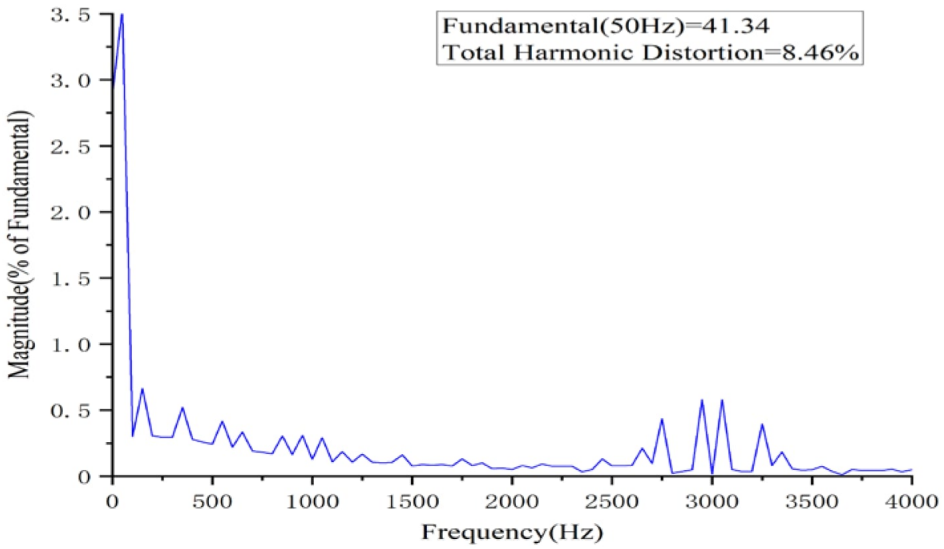

Figure 7. FFT analysis of output current of photovoltaic power generation system.

Table 5. Main harmonic component parameters of the output current of photovoltaic system.

Harmonic Order	Harmonic Content Rate/%	Harmonic Phase/°
1	100	197.5
5	0.65	218.3
7	0.62	11.3
11	0.43	8.9
13	0.34	7.5
17	0.31	6.6
19	0.29	15.2
55	0.45	4.6
59	0.61	−1.2
61	0.61	68.1
65	0.39	46.5

3. Impact of "High-Re-Pe" Distribution Network Harmonics on Grid Line Loss

In High-RE-PE distribution networks, harmonic currents generated when distributed PV systems are connected through power electronic interfaces cause additional losses in lines and distribution transformers. The effects of harmonic frequency differ between these two types of equipment. To provide a computational basis for the subsequent quantification of harmonic losses, this section develops separate harmonic loss models for lines and distribution transformers. The line model primarily considers frequency-dependent variations in the equivalent AC resistance of conductors and corrects their DC resistance for operating temperature. The distribution transformer model primarily considers the effects of harmonic currents on winding resistive losses, winding eddy-current losses, and other stray losses. This section focuses on line and distribution transformer losses caused by harmonic currents and further considers the effects of multiple-harmonic spectra under three-phase unbalanced conditions.

3.1. Component Loss Models Taking into Account Harmonic Factors

3.1.1. Line Harmonic Loss Model

When harmonic currents flow through a line, each frequency component contributes to real power losses. The total line loss is expressed as:

$$P_L = I_1^2 R_1 + I_2^2 R_2 + \cdots + I_h^2 R_h = \sum_{h=1}^{h_{\max}} I_h^2 R_h \tag{14}$$

where I_h is the root-mean-square (RMS) value of the harmonic current of order h, and R_h is the equivalent line resistance at the corresponding frequency. For harmonic order h, the equivalent line resistance accounting for the skin effect is given by [33]:

$$R_h = R_{DC}(1 + y_{s,h}) \tag{15}$$

The skin-effect correction factor $y_{s,h}$ is given by [34]:

$$y_{s,h} = \begin{cases} x_{s,h}^4/(192 + 0.8x_{s,h}^4) \\ (0 < x_{s,h} < 2.8) \\ 0.056x_{s,h}^2 - 0.0177x_{s,h} - 0.136 \\ (2.8 < x_{s,h} \le 3.8) \\ x_{s,h}/2\sqrt{2} - \frac{11}{15} \\ (3.8 < x_{s,h}) \end{cases} \tag{16}$$

When the DC resistance per unit length is expressed in Ω/m, the skin-effect parameter is given by [33]:

$$x_{s,h}^2 = 8\pi f_1 h / R_{DC} \times 10^{-9} \tag{17}$$

where: $y_{s,h}$ denotes the skin effect factor; f_1: denotes the fundamental frequency; h: denotes the harmonic order.

As the temperature of the cable will change during operation, the line DC resistance R_{DC} will change with the temperature change, and according to the literature [35] expression, the correction formula to take into account the temperature change factor is:

$$R_{DC} = R_{dc}[1 + \alpha_T(T_P - 20)] \tag{18}$$

where R_{dc} indicates the DC resistance value when the working temperature of the cable is 20 °C; α_T indicates the temperature correction coefficient, where 0.00393 for copper and 0.00403 for aluminum; T_P indicates the average working temperature of the cable.

3.1.2. Transformer Harmonic Loss Model

The load losses in a distribution transformer consist mainly of winding resistive losses, winding eddy-current losses, and other stray losses [36]:

$$P_{LL} = P + P_{TSL} = P + P_{EC} + P_{OSL} \tag{19}$$

The harmonic losses of distribution lines can be calculated by considering the harmonic current components and the frequency-dependent equivalent resistance of conductors [3].

$$P_{LL} = P_O + F_{HL-EC}P_{EC-O} + F_{HL-OSL}P_{OSL-O} \tag{20}$$

where F_{HL-EC} denotes the eddy current harmonic loss factor of the winding; F_{HL-OSL} denotes the other stray harmonic loss factor. The defining equation is as follows [37]:

$$\begin{aligned} F_{HL-EC} &= \sum_{h=1}^{h_{\max}} I_h^2 h^2 / \sum_{h=1}^{h_{\max}} I_h^2 \\ &= \sum_{h=1}^{h_{\max}} [I_h/I_1]^2 h^2 / \sum_{h=1}^{h_{\max}} [I_h/I_1] \end{aligned} \tag{21}$$

$$\begin{aligned} F_{HL-OSL} &= \sum_{h=1}^{h_{\max}} I_h^2 h^{0.8} / \sum_{h=1}^{h_{\max}} I_h^{0.8} \\ &= \sum_{h=1}^{h_{\max}} [I_h/I_1]^2 h^{0.8} / \sum_{h=1}^{h_{\max}} [I_h/I_1]^{0.8} \end{aligned} \tag{22}$$

where h denotes the harmonic order; I_1 denotes the fundamental current; I_h denotes the hth harmonic current; P_{OSL-O}, P_{EC-O}, P_O indicates the loss of each part caused by the actual measurement amplitude of the current of the electric energy meter under the working frequency of each part, which needs to be multiplied by the correction factor $(I/I_R)^2$ to be determined. In practical engineering, the harmonic current content rate is mostly used for calculation, so the current is transformed as follows [38]:

$$\left(\frac{I}{I_R}\right)^2 = \left(\frac{I_1}{I_R} \times \frac{I}{I_1}\right)^2 = \left(\frac{I_1}{I_R}\right)^2 \times \sum_{h=1}^{h_{\max}} \left(\frac{I_h}{I_1}\right)^2 \tag{23}$$

Under the reference conditions of rated current and rated frequency with no current harmonics, the transformer's rated load losses comprise winding resistive losses, winding eddy-current losses, and other stray losses:

$$P_{LL-R} = P_R + P_{EC-R} + P_{OSL-R} \tag{24}$$

where P_{LL-R} indicates the rated load loss; P_R indicates the loss value of the winding of the transformer when flowing through the rated current. The rated winding resistive losses can

be calculated from the rated currents and DC resistances of the high-voltage and low-voltage windings [39]:

$$P_R = K \times \left(I_{1-R}^2 R_1 + I_{2-R}^2 R_2\right) \tag{25}$$

where I_{1-R}, I_{2-R}: indicate the primary and secondary rated current values; R_1, R_2: indicate the fundamental resistance of the primary and secondary windings, which can be obtained from the test and inspection report. For single-phase transformers K is taken as 1 and for three-phase transformers K is taken as 1.5. The total losses of the distribution transformer considering harmonics are [38]:

$$\begin{aligned} P_T &= P_{NL} + (P_R + F_{HL-EC} P_{EC-R} \\ &\quad + F_{HL-OSL} P_{OSL-R}) \times (I/I_R)^2 \end{aligned} \tag{26}$$

This paper considers harmonics at multiple frequencies generated by distributed PV systems and other equipment connected through power electronic interfaces in High-RE-PE distribution networks. Building on existing line harmonic loss models and distribution transformer load loss models, it consolidates the relationships for calculating losses at different harmonic frequencies. The line model accounts for changes in equivalent resistance caused by conductor temperature and the skin effect. The transformer model considers the frequency characteristics of winding resistive losses, winding eddy-current losses, and other stray losses. It incorporates both harmonic current amplitudes and frequency parameters into the loss calculations. Using line and distribution transformer parameters, loss variations associated with different harmonic orders and levels of individual harmonic content can be quantified separately. The effects of spectra containing multiple harmonics on losses in the two types of equipment can then be compared under the same operating conditions.

3.2. Analysis of the Impact of Harmonics on Grid Line Losses

This section examines the basis for characteristic harmonic mitigation when PV output approaches or exceeds load demand. It compares losses across harmonic orders, examines port differences at equal THD, and analyzes trade-offs in equipment benefits under limited compensation resources.

Equipment parameters used in the analysis are listed in Table 6.

Table 6. Line and transformer parameters.

Harmonic Order	Resistance Value/Ω	Transformer Parameters	Value
5	6.940	Rated capacity/kVA	100
7	6.968	Rated voltage/kV	10/0.4
11	7.052	No-load loss/W	200
13	7.107	Short-circuit loss/W	1500
		Rated current/A	5.77/144.34
		No-load current/%	1.0
		Short-circuit voltage/%	4.0

3.2.1. Effects of Characteristic Harmonic Orders

To distinguish the effects of harmonic order on the additional losses of lines and distribution transformers, the additional loss of equipment X caused by a single hth-order harmonic is defined as follows, with the fundamental current, equipment parameters, and temperature held constant:

$$\Delta P_{X,h} = P_{X,\{1,h\}} - P_{X,\{1\}},\ X \in \{L, T\} \tag{27}$$

Here, L and T denote the line and distribution transformer, respectively. The hth-order harmonic component is extracted from Equation (14) in Section 3.1, and the contribu-

tions are summed according to the three-phase I^2R loss relationship for each frequency component, yielding:

$$\Delta P_{L,h} = \sum_{p\in\{A,B,C\}} R_{h,p} I_{L,h,p}^2 \tag{28}$$

Under three-phase balance, Equation (28) reduces to $3R_h I_{L,h}^2$. Here, $R_{h,p}$ and $I_{L,h,p}$ denote the equivalent resistance and RMS current corresponding to harmonic order h in phase p, respectively. According to Equation (26), transformer losses comprise winding-resistance, eddy-current, and other stray losses; P_R denotes the winding-resistance loss at rated current. The resulting three-phase single-frequency losses are presented in Figures 8 and 9.

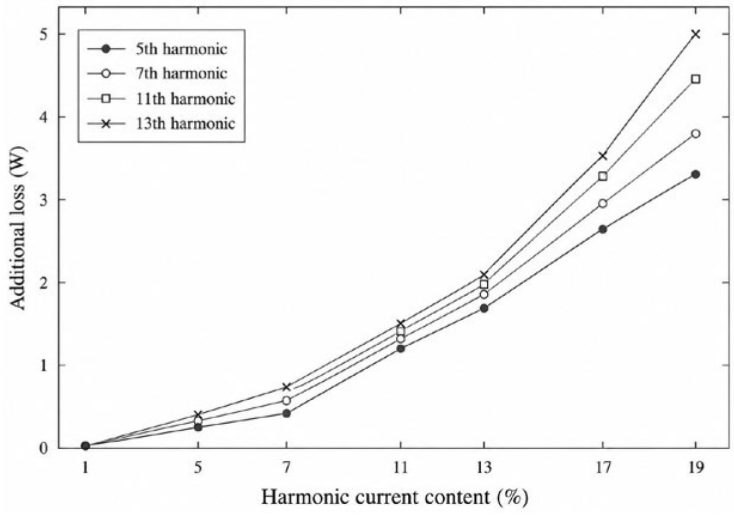

Figure 8. Additional line losses at different harmonic orders and current contents.

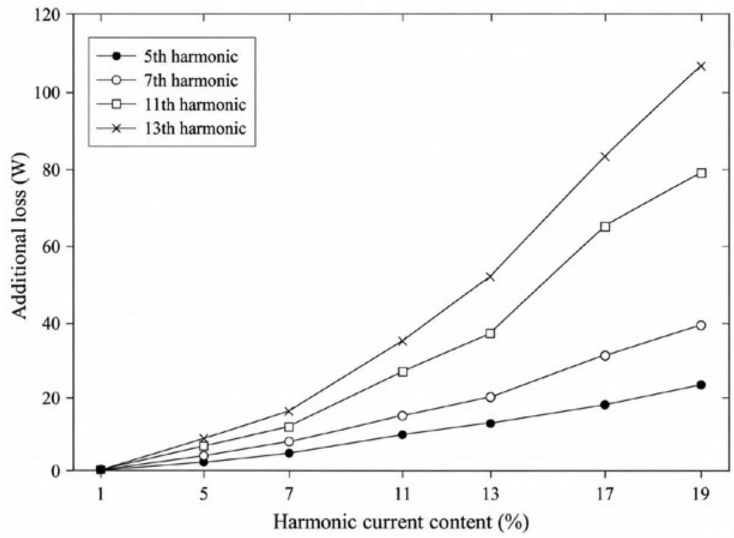

Figure 9. Additional distribution transformer losses at different harmonic orders and current contents.

At a given harmonic current content, the additional losses of both devices increase with harmonic order, with a more pronounced increase for the distribution transformer. At a 19% harmonic current content, the 5th- and 13th-order harmonics produce line losses of 3.25 and 4.99 W and transformer losses of 21.54 and 105.48 W, respectively. This device-dependent frequency response motivates comparing line and transformer terminal responses for different spectral compositions at the same three-phase aggregated THD calculated from the four harmonic components.

3.2.2. Port Differences at Equal THD

The additional transformer load loss caused by harmonics depends not only on the harmonic current amplitudes but also on the harmonic-order distribution. Therefore, different spectral compositions may produce different losses even when the overall current harmonic distortion level is the same [40]. For three-phase systems, the RMS values of the fundamental and harmonic currents in each phase can be used to analyze harmonics and line losses [41]. Accordingly, to distinguish the effects of spectral composition and overall distortion level on losses under the simultaneous action of multifrequency harmonics, the 5th-, 7th-, 11th-, and 13th-order harmonics are selected to define a four-frequency three-phase aggregated current distortion ratio:

$$\mathrm{THD}_{4,3\phi} = \sqrt{\frac{\sum_{p\in\{A,B,C\}}\sum_{h\in H}\left|\bar{I}_{\mathrm{PV},p,h}\right|^2}{\sum_{p\in\{A,B,C\}}\left|\bar{I}_{\mathrm{PV},p,1}\right|^2}},\ H=\{5,7,11,13\} \tag{29}$$

Here, $\bar{I}_{\mathrm{PV},p,h}$ and $\bar{I}_{\mathrm{PV},p,1}$ denote the RMS phasors of the harmonic current of order h and the fundamental current in phase p, respectively, and H denotes the set of selected characteristic harmonic orders. The C1 spectrum was obtained from the three-phase harmonic spectra of a grid-connected PV inverter under moderate irradiance [42], while C2 was based on three-phase harmonic current data from a grid-connected PV plant [43]. Both datasets represent practical PV grid-connected operating conditions relevant to this study.

Taking the aggregated THD of C1 as the target, the characteristic harmonic-current components in C2 are scaled by a common factor. The scaling factor is given by:

$$\alpha = \frac{\mathrm{THD}_{4,3\phi,\mathrm{C1}}}{\mathrm{THD}_{4,3\phi,\mathrm{C2}}} = 0.309849 \tag{30}$$

For $h \in H$, the harmonic-current phasor of C3 is set to α times the corresponding component of C2, while the fundamental component remains unchanged. Because $\alpha > 0$, this scaling preserves the harmonic phase-angle relationships and the relative characteristics of the three phases. Consequently, C3 and C1 have the same four-frequency three-phase aggregated THD. The three cases are implemented in the engineering equivalent model shown in Figure 10.

To compare the equipment responses, harmonic currents are extracted from the high-voltage line and the low-voltage side of the distribution transformer.

$$\begin{aligned} P_{L,R1} &= R_1 \sum_{p\in\{A,B,C\}}\sum_{h\in H}\left|\bar{I}_{\mathrm{Line},p,h}\right|^2 \\ K_{EC} &= \frac{1}{3I_R^2}\sum_{p\in\{A,B,C\}}\sum_{h\in H} h^2\left|\bar{I}_{T,p,h}\right|^2 \\ K_{OSL} &= \frac{1}{3I_R^2}\sum_{p\in\{A,B,C\}}\sum_{h\in H} h^{0.8}\left|\bar{I}_{T,p,h}\right|^2 \end{aligned} \tag{31}$$

Here, $R_1 = 6.78972\ \Omega$ denotes the power-frequency resistance per phase of the 20-km line, I_R denotes the rated phase current on the low-voltage side of the distribution transformer, $P_{L,R1}$ denotes the line comparison metric, and K_{EC} and K_{OSL} denote the dimensionless frequency-weighting indices for the transformer eddy-current loss and other stray-load loss, respectively. To identify the harmonic orders responsible for differences in terminal responses, the contribution of each harmonic order is defined as follows (as shown in Figure 11):

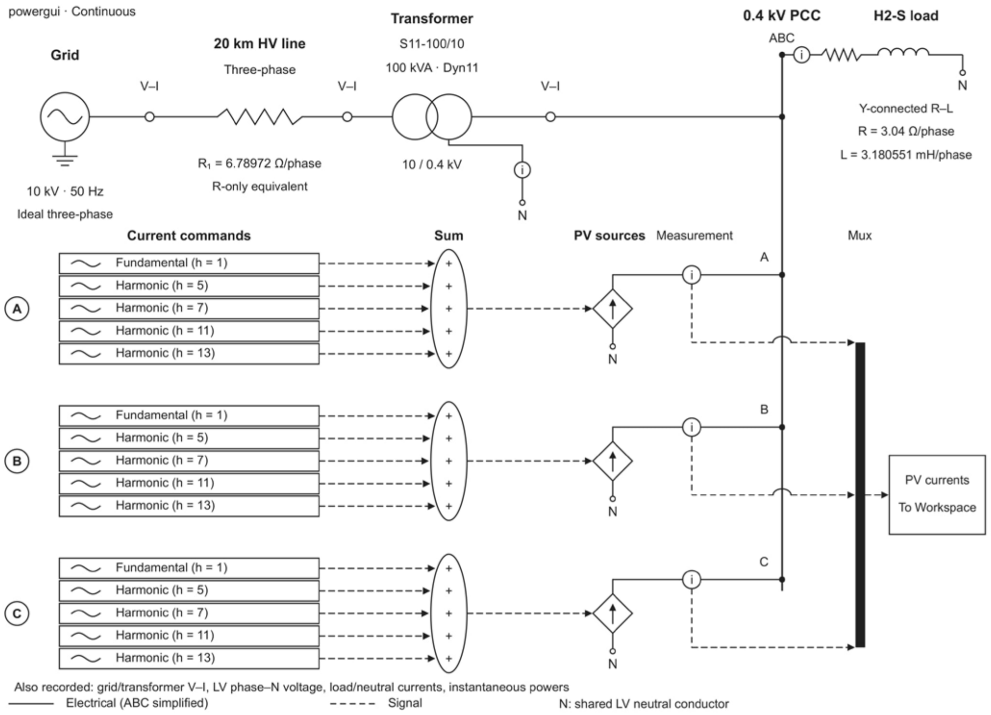

Figure 10. Detailed Simulink model for three-phase PV harmonic-current injection and data acquisition.

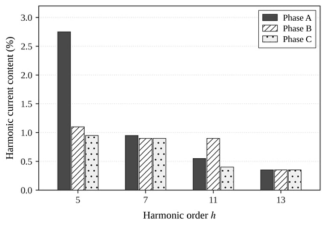

(**a**) Three-Phase Harmonic Content in C1

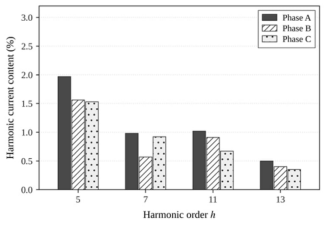

(**b**) Three-Phase Harmonic Content in C3

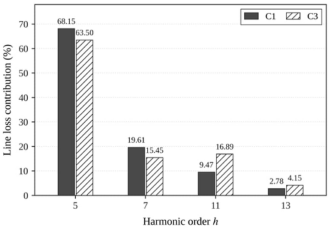

(**c**) Harmonic Contributions to Line Loss

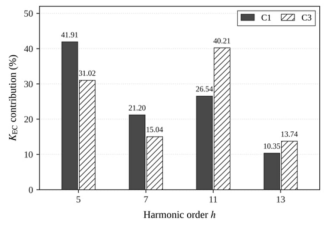

(**d**) Harmonic Contributions to Transformer KEC

Figure 11. Comparison of Harmonic Spectra and Loss Characteristics at Equal Aggregated THD.

Under the 45 kW M0 condition, changing the spectrum from C1 to C3 increased the 11th-order contribution to K_{EC} from 26.54% to 40.21%. Meanwhile, $P_{L,R1}$ and K_{EC} increased by 7.04% and 21.65%, respectively. These results show that equal aggregated THD does not imply identical equipment-level responses; harmonic spectrum and port characteristics should also be considered in harmonic-mitigation assessment.

3.2.3. Harmonic Compensation Allocation and Equipment-Level Metric Comparison Under a Fixed Budget

To analyze the effects of different harmonic-allocation strategies on line and distribution-transformer metrics under limited compensation resources, this study follows the concept of allocating harmonic components by order under limited compensation capacity [44]. An uncompensated case, M0, and three ideal compensation strategies, M1–M3, are then

defined. Taking 45 kW as the reference operating condition, the PV-output scaling factor is defined as $s = P_{\text{nom}}/(45\text{kW})$. Assuming that the current at each harmonic order scales proportionally with the PV output, the sum of the squared RMS currents across the three phases for harmonic order h is given by:

$$b_h(s) = \sum_{\phi\in\{A,B,C\}} \left|I_{\text{PV},\phi,h}(s)\right|^2 = s^2 b_h(1) \tag{32}$$

Let ah denote the compensation ratio for harmonic order h. For a given harmonic order, the same ah is applied to all three phase components. A fixed absolute compensation budget is defined as 25% of the sum of the squared RMS currents of the four characteristic harmonics across the three phases under the 45-kW operating condition with the C1 spectrum and the uncompensated case M0, namely:

$$B_0^2 = 0.25\sum_{h\in H} b_h(1) = 1.4604\text{A}^2 \tag{33}$$

Here, H = {5, 7, 11, 13}. The same absolute compensation budget is used for all PV output levels and spectral cases. Because C1 and C3 have the same four-frequency three-phase aggregated THD, they have the same equivalent compensation-budget ratio relative to the total harmonic current, given by $\beta_{\text{eff}} = 0.5/s$.

The three strategies use equal-weight allocation (M1), higher-order harmonic weighting (M2), and line-response weighting (M3), respectively. M3 is calibrated using the line response under the 45-kW operating condition, the C1 spectrum, the H2-S load, and the M0 uncompensated case. The resulting weights are then kept unchanged under all other operating conditions. The weights for the three strategies are defined as follows:

$$\begin{aligned} &\text{M1}: \quad w_h = 1 \\ &\text{M2}: \quad w_h = \left(\tfrac{h}{5}\right)^2 \\ &\text{M3}: \quad w_h = \tfrac{q_h}{q_5},\ q_h = \tfrac{R_1\sum_{\phi}\left|I_{\text{line},h,\phi}\right|^2}{b_h(1)} \end{aligned} \tag{34}$$

M3 assigns weights of 1.0000, 1.1035, 1.0428, and 1.0932 to the 5th-, 7th-, 11th-, and 13th-order harmonics, respectively, and keeps these weights unchanged under all subsequent operating conditions. With the objective of minimizing the weighted sum of the squared source-side residual harmonic currents, the following optimization model is formulated subject to a fixed absolute compensation-budget constraint:

$$\begin{aligned} &\min_{\{a_h\}} \quad \sum_{h\in H} w_h b_h(s)(1-a_h)^2 \\ &\text{s.t.} \quad\ \ \sum_{h\in H} b_h(s)a_h^2 \le B_0^2,\ 0 \le a_h \le 1 \end{aligned} \tag{35}$$

When the compensation budget is insufficient to completely eliminate the target harmonics, the compensation-budget constraint is binding at the optimum. The compensation ratio for each harmonic order is then given by:

$$a_h = \frac{w_h}{w_h+\mu},\ \sum_{h\in H} b_h(s)\left(\frac{w_h}{w_h+\mu}\right)^2 = B_0^2 \tag{36}$$

Here, $\mu > 0$ denotes the Lagrange multiplier associated with the budget constraint. The line comparison metric $P_{L,R1}$ and the distribution-transformer frequency-weighting index K_{EC} are calculated according to (31). Taking the M0 case with the same PV output and spectrum as the baseline, the relative reduction rates of these two metrics are defined as follows:

$$\eta_Q = \frac{Q_{\text{M0}} - Q_{\text{M}i}}{Q_{\text{M0}}} \times 100\%,\ Q \in \{P_{L,R_1}, K_{\text{EC}}\},\ i = 1,2,3 \tag{37}$$

As shown in Table 7, M1 and M3 achieve similar reductions in the line comparison metric and the distribution-transformer frequency-weighting index, whereas M2 exhibits a different pattern of improvement. For example, in the 45-kW C3 case, the reduction rate of the transformer frequency-weighting index increases from 75.00% with M1 to 81.00% with M2, whereas that of the line comparison metric decreases from 75.00% to 69.93%. These results indicate that increasing the weights assigned to higher-order harmonics does not necessarily yield greater reductions in both metrics simultaneously.

Table 7. Comparison of line and transformer index reductions under a fixed compensation budget.

PV Output	Spectrum	Index	M1 (%)	M2 (%)	M3 (%)
45.00	C1	$P_{L,R1}$	75.00	72.07	75.02
		K_{EC}	75.00	79.81	75.40
45.00	C3	$P_{L,R1}$	75.00	69.93	74.97
		K_{EC}	75.00	81.00	75.42
54.15	C1	$P_{L,R1}$	65.84	62.01	65.86
		K_{EC}	65.84	71.71	66.30
54.15	C3	$P_{L,R1}$	65.84	59.55	65.80

As PV output increases from 45 to 54.15 kW, the equivalent compensation-budget ratio decreases. The compensation ratio for M1 falls from 50% to 41.55%, while the reduction rates of both equipment metrics fall from 75.00% to 65.84%. In addition, weighted compensation yields different reductions in the equipment metrics for C1 and C3 despite their equal aggregated THD, indicating that spectral composition also affects the degree of metric improvement. Harmonic mitigation in distribution networks incorporating distributed PV should therefore consider the overall distortion level, variations in PV output, harmonic spectral distribution, and the harmonic-order response characteristics of lines and distribution transformers when allocating limited compensation resources. These findings provide an analytical basis for subsequent selective compensation of characteristic harmonics.

4. APF–LCLLC Based Filter Circuit Model

4.1. APF–LCLLC Filter Circuit Analysis

Both the grid-connected distributed photovoltaic (PV) system and the three-phase rectifier load can introduce harmonics. To address grid-side current distortion when these sources coexist, a shunt active power filter (APF) is employed to inject compensating current at the grid connection point, thereby reducing the harmonic components flowing into the grid. This configuration is suitable for current harmonic mitigation in systems with both PV generation and nonlinear loads. The APF power stage employs a three-phase two-level voltage-source bridge, with three-phase compensating currents regulated through pulse-width modulation (PWM) [45].

As the selected characteristic harmonics occur at multiple frequencies, the current loop employs combined proportional–integral (PI) and quasi-proportional–resonant (quasi-PR) control. The quasi-PR controller regulates the tracking errors at the target harmonic frequencies, while the PI controller regulates the remaining error, aligning the active control structure with the requirements for multiharmonic compensation. To accommodate both the compensation of selected harmonics and the suppression of APF switching ripple, an APF–LCLLC hybrid filtering structure is adopted. The AC output of the APF is connected to the grid connection point through the LCLLC filter, with the overall structure connected in parallel with the load, as shown in Figure 12.

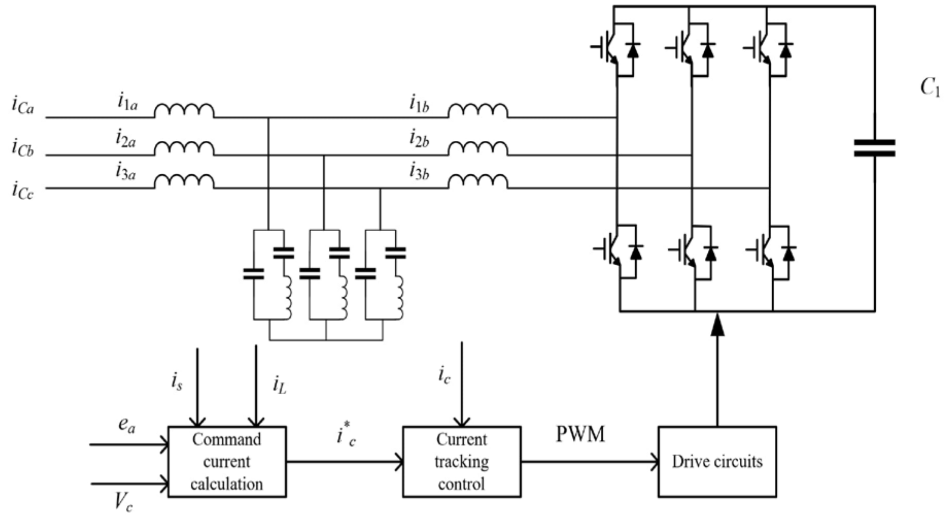

Figure 12. APF–LCLLC basic structure diagram.

In distribution networks with high penetration of renewable energy and power electronic equipment (High-RE-PE), characteristic harmonics from nonlinear loads coexist with switching ripple from power electronic devices, creating harmonic mitigation requirements across different frequency bands. Accordingly, the LCLLC filter is designed with separate configurations for the main LCL section and the additional LC branch. The main LCL section retains the existing parameters, with L_1 and L_2 set to 2 mH and 0.35 mH, respectively, and the filter capacitor C_d set to 2 μF. The additional LC branch consists of $L_f = 31.69$ μH and $C_f = 2$ μF, corresponding to a series-resonant frequency of approximately 20 kHz, in accordance with the design objective of matching the APF switching frequency. This branch is intended to attenuate APF switching ripple, complementing the compensation of selected characteristic harmonics by the APF through a division of filtering functions across frequency bands.

4.2. Joint Control Strategy Based on Pi and Quasi-Pr

To address the 5th, 7th, 11th, and 13th characteristic harmonics in grid-connected distributed PV systems, this paper employs combined PI and quasi-PR control within the APF–LCLLC topology, drawing on the concept of multi-resonant selective harmonic compensation [46]. Building on the harmonic spectral analysis in Section 3.2, an averaged model is used to examine harmonic reduction, compensating current demand, and the response to harmonic switching under the existing control parameters, providing a consistent baseline for subsequent parameter comparisons and operating-condition validation.

Let r denote the harmonic compensation reference current and ig the feedback current. The quantities rH and y_H represent the target harmonic components of the reference and feedback signals, respectively. The tracking error is decomposed into the target harmonic error eR and the residual error ePI, which are regulated by the quasi-PR and PI controllers, respectively. The outputs of the two controllers are then summed, yielding the following control law:

$$\begin{aligned} &e = r - i_g,\ e_R = r_H - y_H \\ &e_{\mathrm{PI}} = (r - r_H) - (i_g - y_H) = e - e_R \\ &u_{\mathrm{ctrl}} = G_{\mathrm{PI}}(s)e_{\mathrm{PI}} + G_R(s)e_R \end{aligned} \tag{38}$$

The PI and quasi-PR controllers adopt proportional–integral and finite-bandwidth resonant forms, respectively. With reference to the controller designs and parameter settings reported in [47,48], this study adopts a baseline parameter set, P0. The proportional and integral gains of the PI controller are 6.1 and 32.5, respectively. The quasi-PR controller has

a common proportional gain of 0.05, a resonant gain of 3 for each branch, and a bandwidth parameter of 10 rad/s. The corresponding transfer functions are expressed as follows:

$$\begin{aligned} G_{\mathrm{PI}}(s) &= 6.1 + \tfrac{32.5}{s} \\ R_h(s) &= \frac{2K_{r,h}\omega_c s}{s^2 + 2\omega_c s + \omega_h^2} \\ G_R(s) &= 0.05 + \sum_{h\in\mathcal{H}} R_h(s),\ \mathcal{H} = \{5,7,11,13\} \end{aligned} \tag{39}$$

The resonant angular frequency of each branch is defined as ω_h = 2 πhf$_1$, where f$_1$ = 50 Hz is the fundamental frequency. The corresponding resonant frequencies for the 5th, 7th, 11th, and 13th harmonics are 250, 350, 550, and 650 Hz, respectively. To separate the target harmonic error from the residual tracking error, a multi-frequency complementary filter is employed, with the following transfer functions and error decomposition relationships:

$$\begin{aligned} F_P(s) &= \prod_{h\in\mathcal{H}} \frac{s^2 + \omega_h^2}{s^2 + 2\omega_e s + \omega_h^2} \\ F_R(s) &= 1 - F_P(s) \\ e_{\mathrm{PI}} &= F_P(s)e,\ e_R = F_R(s)e \\ \omega_e &= 10\ \mathrm{rad/s} \end{aligned} \tag{40}$$

$$G_{PI}(S) = K_P + K_i/S \tag{41}$$

Based on the above control law and multi-frequency complementary error decomposition, the combined PI–quasi-PR control scheme is illustrated in Figure 13.

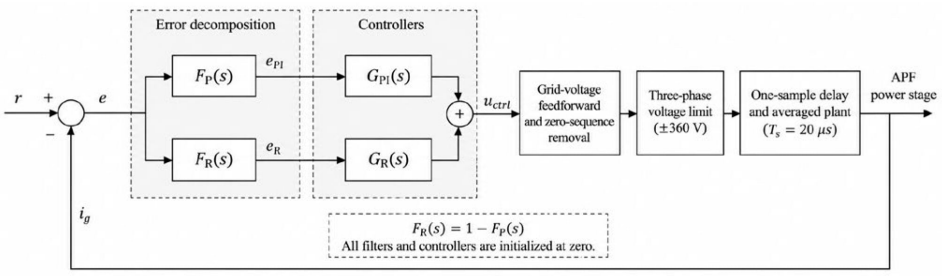

Figure 13. Block diagram of the combined PI–quasi-PR control scheme.

To compare the control responses of the baseline parameter set P0 and its perturbed variants under different harmonic spectra, an averaged model based on the control structure shown in Figure 13 is adopted. The model operates with a 380 V AC grid and a constant DC-link voltage of 800 V, with a sampling period of 20 μs. Two harmonic input cases, D1 and D2, are reconstructed as balanced three-phase cases based on measured harmonic data from grid-connected PV systems reported in [42,43]. Both cases have a fundamental current of 10 A RMS per phase and a four-frequency three-phase aggregated current THD of approximately 6.93%, allowing the effects of different harmonic spectral compositions on compensation responses to be compared at the same aggregated distortion level.

For each of the D1 and D2 operating cases, the harmonic input, power stage, and actuation constraints are kept unchanged when comparing the baseline parameter set P0 with five perturbed parameter sets, as detailed in Table 8. The steady-state evaluation window is set to 3.0–3.2 s. The RMS compensating current is defined as the maximum of the three phase RMS values of the grid-side current i_g over the specified evaluation window. The residual harmonic level is quantified by the combined magnitude of the four selected harmonic currents across the three phases at the PCC, expressed as a percentage of its uncompensated value. The four-frequency current distortion ratio is calculated relative to the fundamental

current in each operating case. These metrics are used to evaluate the effects of variations in resonant gain, bandwidth, and PI gains on harmonic compensation performance.

Table 8. Steady-state compensation performance of different parameter sets in case D1.

Parameter Set	Parameter Variation	Residual Harmonic Ratio E_H (%)	Compensating Current RMS (A)
P0	Baseline	82.35	0.5097
P1	Kr = 1.5	92.71	0.4039
P2	Kr = 6	62.71	0.6400
P3	ω_c = 5 rad/s	82.50	0.5105
P4	ω_c = 20 rad/s	82.06	0.5082
P5	PI gains −20%	82.66	0.5653

Table 8 shows that increasing the resonant gain from 3 under P0 to 6 under P2 reduces the aggregate residual ratio across the four harmonic frequencies from 82.35% to 62.71%, while increasing the RMS compensating current by approximately 25.6%. This result illustrates the trade-off between harmonic suppression and compensation-current requirements in this case study. To further assess nominal closed-loop stability and the response at the target harmonic frequencies under the baseline parameter set P0, a discrete-time closed-loop analysis of the averaged model is performed. The corresponding sensitivity function is given by:

$$\begin{aligned} C_{\mathrm{eq}}(s) &= G_{\mathrm{PI}}(s)F_P(s) + G_R(s)F_R(s) \\ S_d(z) &= \frac{1}{1+P_d(z)z^{-1}C_{\mathrm{eq},d}(z)} \end{aligned} \tag{42}$$

Here, $P_d(z)$ denotes the discrete-time transfer function of the averaged power stage, and $C_{\mathrm{eq},d}(z)$ denotes the equivalent discrete-time controller. Under P0, the maximum closed-loop pole magnitude is approximately 0.999897, and the sensitivity magnitudes at the four target harmonic frequencies range from 0.761 to 0.978. This result indicates that the closed-loop system with parameter set P0 is stable under the nominal linear model and can attenuate the target harmonics.

The series resistance in the LCLLC capacitor branch provides damping, while the grid impedance and the active control loop incorporating sampling delay jointly affect the closed-loop response. Discrete parameter sweeps are conducted for additional grid inductance (0–1.6 mH) and grid resistance (0–0.2 Ω), as well as component tolerances of ±10% for inductors and capacitors and ±5% for the damping resistor. The results show that all poles of the unsaturated linear closed-loop models with P0 and P2 remain inside the unit circle. Attenuation is maintained at all four target harmonic frequencies under component tolerances. However, localized amplification occurs under certain grid-impedance conditions, with maximum residual amplitude ratios of 1.097 and 1.009 for P0 and P2, respectively.

To further examine compensation responses under different harmonic spectra and dynamic switching conditions, P0 and P2 are compared in cases D1, D2, and E1. The results are presented in Figure 14 and Table 9.

As shown in Figure 14 and Table 9, P0 reduces the aggregate amplitude of the harmonic currents at the four frequencies by 17.65% and 17.59% in cases D1 and D2, respectively. The RMS compensating current is approximately 0.510 A in both cases. These results indicate that P0 exhibits similar steady-state compensation responses under the two harmonic spectra considered.

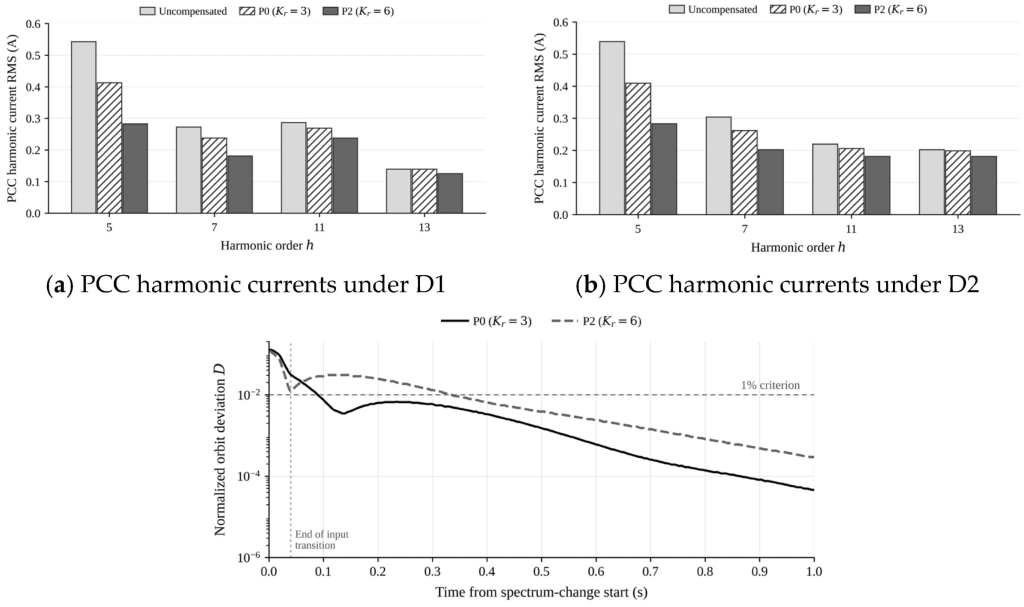

(**a**) PCC harmonic currents under D1

(**b**) PCC harmonic currents under D2

(**c**) Spectrum-switching recovery under E1

Figure 14. Harmonic compensation and spectrum-switching responses.

Table 9. Steady-State Compensation and Spectrum-Switching Recovery of P0 and P2.

Parameter Set	Residual Harmonic Ratio E_H (%)	RMS Compensating Current (A)	Recovery Time (s)	Spectral-Transition Recovery Time (s)	Load-Change Recovery Time (s)
P0	82.41	0.5098	0.08	0.18	0.54
P2	62.78	0.6403	0.32	0.42–0.46	0.62

Recovery is defined by a normalized deviation ($D \leq 0.01$) sustained for five consecutive fundamental-frequency cycles, with no further violations during the remaining observation period. In Table 9, the original recovery time is measured from the event onset to the start of the first qualifying cycle, whereas the spectral-transition and load-change recovery times are measured to the end of the fifth qualifying cycle. Under the selected representative grid-impedance and component-tolerance conditions, P0 achieves confirmed recovery earlier than P2 following spectral transitions. P0 also recovers faster when the load current steps from 8 A to 10 A and then rises to 12 A over 20 ms. With the DC-side voltage held constant at 800 V, both parameter sets achieve confirmed recovery within 0.12 s after the equivalent current reference decreases from 2 A to 0 A. This case is used only to evaluate the response to a reference-command disturbance.

In case D2, P0 requires approximately 20.4% less compensation current than P2. Although P2 achieves lower residual harmonic levels at steady state, P0 offers a better balance between compensation-current requirements and dynamic recovery. As the penetration of distributed PV and power electronic equipment increases, harmonics from multiple sources and changes in operating conditions place greater demands on the current capacity and dynamic tracking capability of compensation devices. The lower compensation-current requirements and rapid recovery exhibited by P0 better suit the operating requirements considered in this study, which extend beyond minimizing steady-state residual harmonic levels alone. P0 is therefore selected as the baseline parameter set for subsequent evaluation of the APF–LCLLC hybrid filtering system.

5. Simulation and Analysis of Harmonic Management with Distributed PV

5.1. Simulation Construction of a Filter Circuit with Distributed Photovoltaic

To evaluate the harmonic mitigation performance of the APF–LCLLC hybrid filter in the presence of distributed PV generation and nonlinear loads, a system-level simulation model is developed in MATLAB/Simulink (2019). Three operating conditions are compared: without compensation, with APF compensation alone, and with APF–LCLLC hybrid compensation. The model uses a three-phase AC supply with a line-to-line voltage of 380 V and a three-phase uncontrolled rectifier as the nonlinear load. The APF controller uses the baseline parameter set P0. In the APF-only and APF–LCLLC compensation cases, the APF rated capacity, current limit, and controller parameters are kept identical to compare the overall harmonic compensation performance of the system with and without the LCLLC filter branch. The system simulation model, corresponding functional structure, and APF controller model are shown in Figures 15–17, respectively.

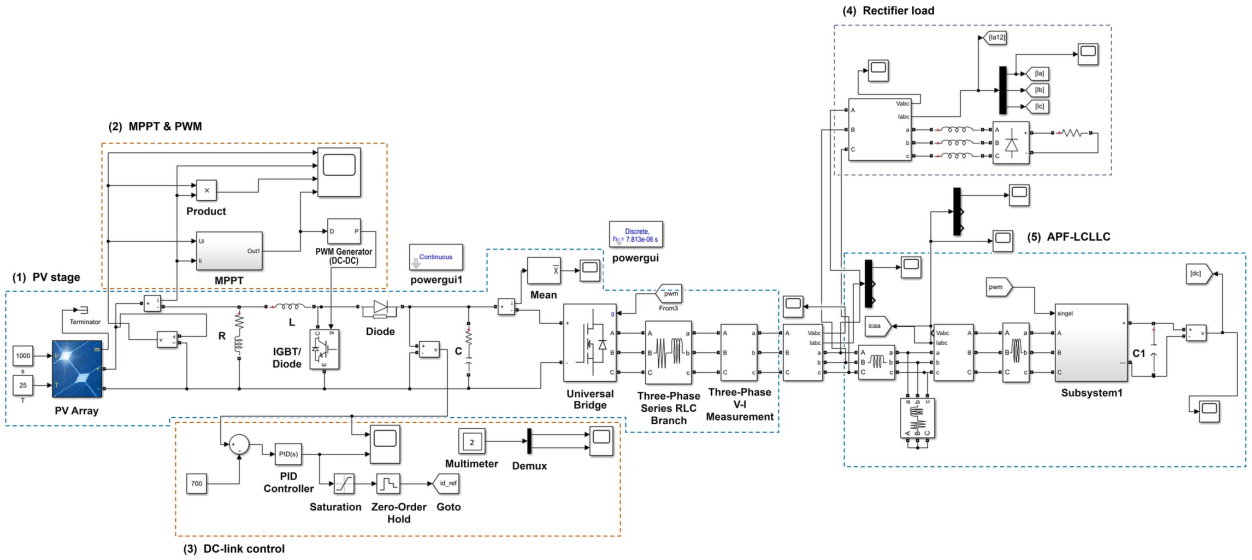

Figure 15. APF–LCLLC system simulation model.

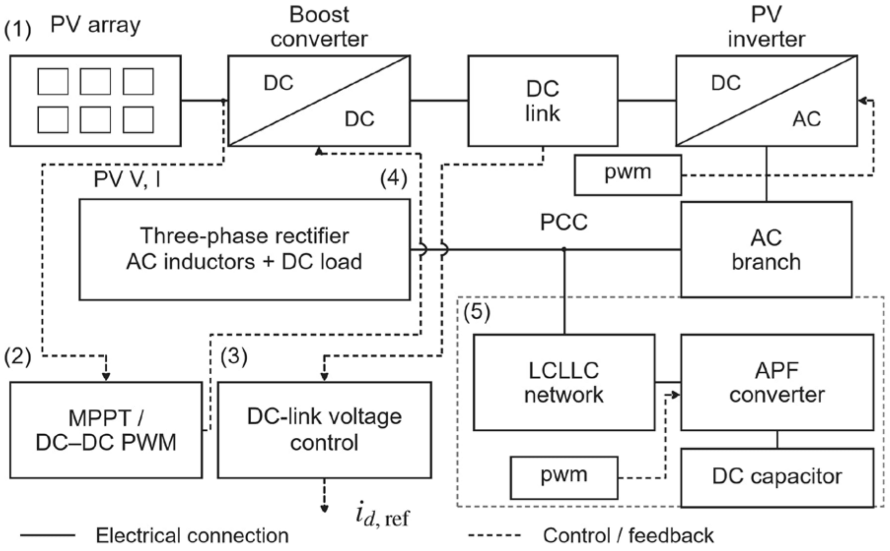

Figure 16. Functional structure of the APF–LCLLC system.

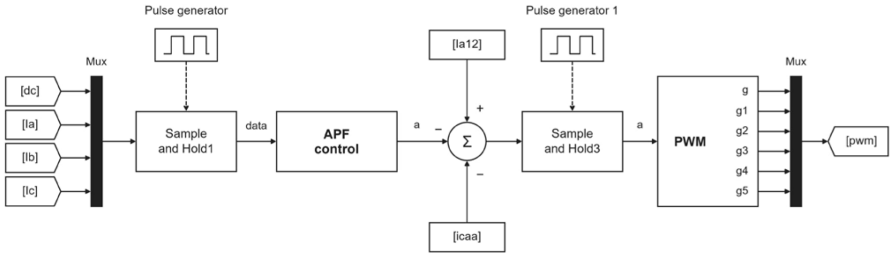

Figure 17. APF controller simulation model.

With reference to the technical requirements for active power filters in GB 51204–2016 [49], a current THD level of 5% is adopted as a comparison reference for the 380 V system to evaluate harmonic compensation performance under three conditions: uncompensated, APF-only, and APF–LCLLC.

5.2. Simulation Results and Analyses

Figure 18 shows the system current waveform with APF compensation alone. The APF is activated at 0.1 s.

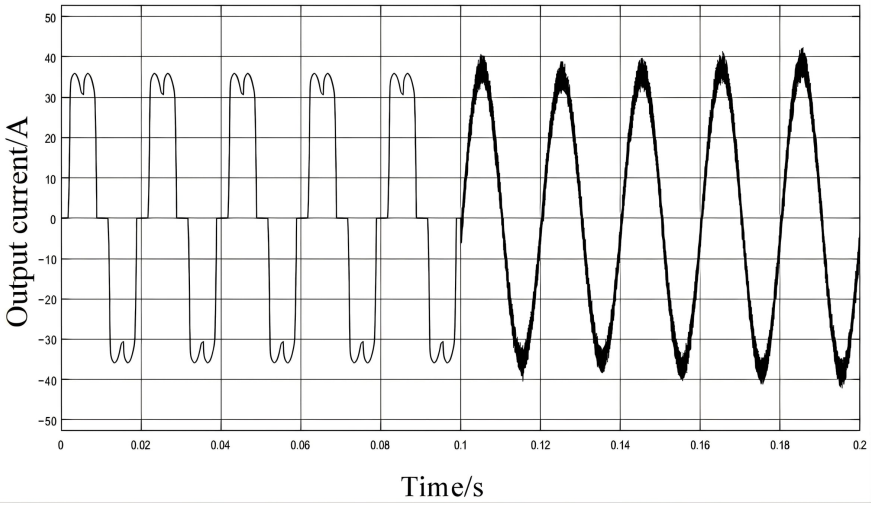

Figure 18. Load current output waveform after inputting APF.

As shown in Figure 18, the system current waveform exhibits marked distortion before APF activation. After the APF is activated at 0.1 s, the waveform more closely resembles a sine wave, indicating that the APF mitigates harmonics to some extent under this operating condition. However, residual ripple remains visible. To further quantify the harmonic levels before and after compensation, spectral analysis is performed on the current. The current spectrum under uncompensated operation is shown in Figure 19.

As shown in Figure 19, the THD of the uncompensated system current is 27.50%, exceeding the 5% reference value used for evaluation. High harmonic distortion degrades power quality and may cause fluctuations in system operation. To further evaluate the harmonic suppression performance of the APF, Figure 20 presents the current spectrum with APF compensation alone for comparison with the uncompensated results.

The FFT spectrum in Figure 20 shows that, with APF compensation alone, the THD of the system current decreases from 27.50% to 3.74%, below the 5% reference value used for evaluation. However, characteristic harmonics of orders $6k \pm 1$ are not fully suppressed.

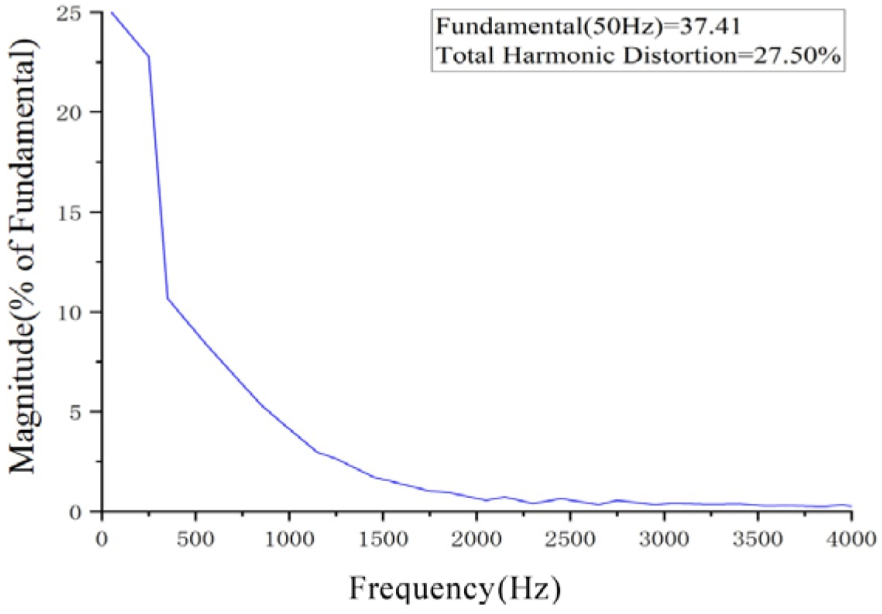

Figure 19. Load current waveform FFT.

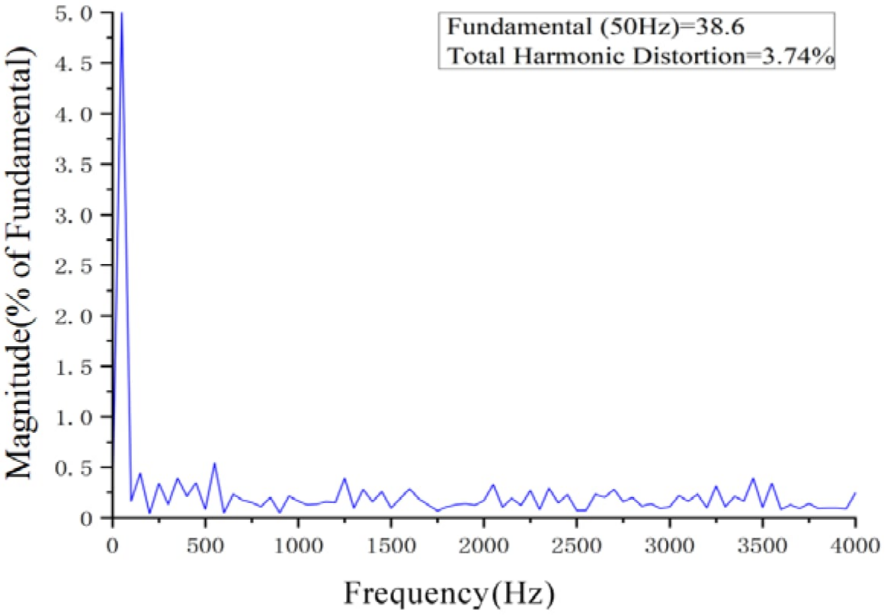

Figure 20. Spectrum analysis after APF compensation.

In the APF–LCLLC hybrid filter, the LCLLC branch attenuates higher-order harmonics, while the APF compensates the remaining harmonic components, enabling effective suppression of medium- and high-frequency harmonics. The simulated system current waveform with APF–LCLLC hybrid compensation is shown in Figure 21, and the corresponding harmonic spectrum is shown in Figure 22.

As shown in Figure 21, the load-current waveform at the output of the filter circuit exhibits less distortion and appears smoother with APF–LCLLC hybrid compensation than with APF compensation alone. These observations indicate improved filtering performance of the APF–LCLLC hybrid filter under this operating condition.

As shown in Figure 22, the current THD is reduced to 1.53% with APF–LCLLC hybrid compensation in the simulated distribution network under High-RE-PE conditions, below the 5% reference value used for evaluation. Under combined PI and quasi-PR control,

the individual harmonic contents at orders 5, 7, 11, and 13 in the $6k \pm 1$ sequence are substantially reduced.

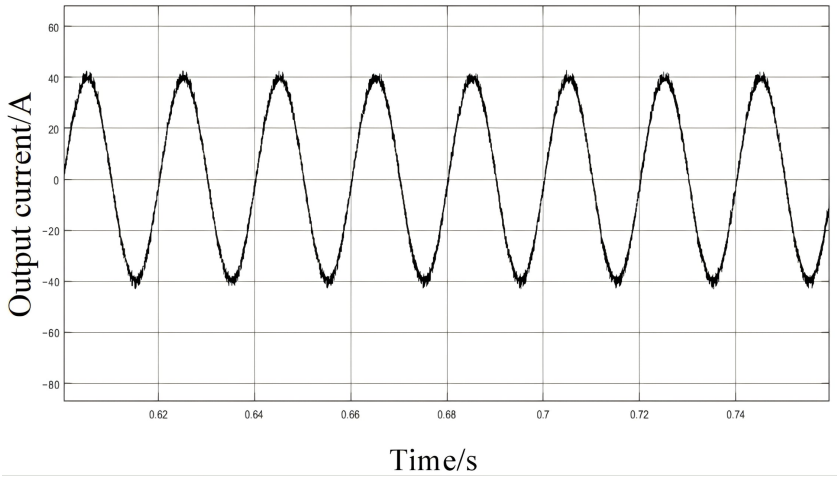

Figure 21. Load current output waveform after investment APF–LCLLC.

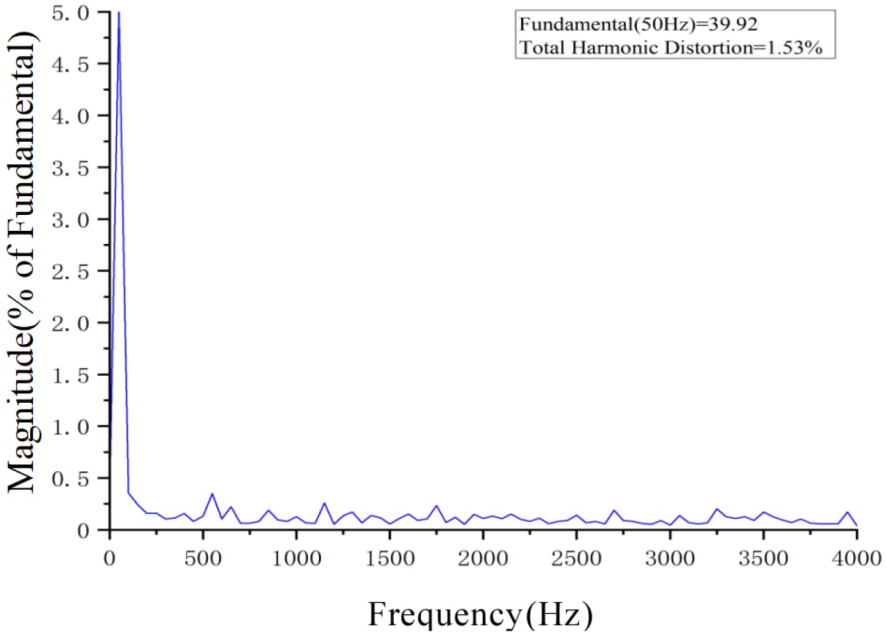

Figure 22. Spectrum analysis after APF–LCLLC compensation.

System-level simulation results show that the APF–LCLLC hybrid filter further improves the current waveform and reduces harmonic content in the current spectrum when distributed PV generation and nonlinear loads are both present. Compared with APF compensation alone, the current THD decreases from 3.74% to 1.53%, corresponding to a relative reduction of approximately 59.1%. These results indicate better harmonic suppression performance of the hybrid filter under the operating condition examined.

Previous research has combined LR–CR and SAPF to suppress harmonics in different frequency bands [50]. This section demonstrates the compensation performance of the APF–LCLLC configuration with the specified control parameters. In the examined case involving both PV generation and nonlinear loads, current THD decreases from 3.74% with APF compensation alone to 1.53% with APF–LCLLC compensation. The current waveform and harmonic spectrum are further improved. These results demonstrate the additional filtering effect obtained by incorporating LCLLC. This configuration provides a

viable hybrid filtering scheme for mitigating novel harmonics in High-RE-PE distribution networks with distributed PV.

6. Conclusions

This study addresses harmonic mitigation needs in High-RE-PE distribution networks incorporating both distributed PV generation and nonlinear loads. It investigates harmonic characteristics, the effects of harmonics on equipment losses, and an APF–LCLLC compensation strategy. The following conclusions are drawn from theoretical analysis and numerical simulations:

(1) A grid-connected PV simulation model is developed to account for the effects of irradiance and temperature. In the operating conditions studied, analysis of multiple harmonic sources shows that characteristic harmonics coexist with components near the switching frequency. The characteristic harmonics include the 5th, 7th, 11th, and 13th harmonics of the $6k \pm 1$ sequence. These findings identify the priority harmonic orders for equipment loss analysis and selective compensation. They also clarify the need for characteristic harmonic compensation and higher-frequency harmonic attenuation.

(2) Harmonic loss models for lines and distribution transformers are used to examine how harmonic current content, harmonic order, and spectral composition affect equipment responses. In the single-frequency cases, when the individual harmonic content in each device current is 19%, the 5th and 13th harmonics produce additional line losses of 3.25 W and 4.99 W, respectively. The corresponding additional distribution transformer losses are 21.54 W and 105.48 W. For the selected characteristic harmonics, comparisons at the same aggregated THD show that the line comparison metric and transformer frequency-weighting index still vary with spectral composition. With a fixed compensation budget, different compensation allocations among harmonic orders involve trade-offs between improvements in the two indicators. These results indicate that spectral composition and equipment responses should be considered alongside overall distortion when allocating harmonic compensation resources.

(3) An APF–LCLLC hybrid filtering strategy is proposed to combine selective compensation of characteristic harmonics with attenuation of higher-frequency harmonics. The strategy divides filtering tasks between the active and passive filters by frequency band and uses complementary decomposition of the tracking error in PI–quasi-PR control. This enables targeted regulation of the 5th, 7th, 11th, and 13th characteristic harmonics. Comparisons using different controller parameter sets further clarify the trade-offs among steady-state harmonic suppression, compensation current requirements, and dynamic recovery. System simulations are conducted for operating conditions with both distributed PV generation and nonlinear loads. In the examined cases, APF–LCLLC compensation using the baseline controller parameters further suppresses the selected characteristic harmonics, as well as other residual components within the frequency range shown. Current THD decreases to 1.53%, considerably lower than the 3.74% obtained with APF compensation alone, and the current waveform is further improved. This strategy provides a new approach to mitigating novel harmonics in High-RE-PE distribution networks where harmonics from multiple sources coexist at multiple frequencies.

MATLAB/Simulink (2019) simulations have demonstrated the harmonic compensation performance of the APF–LCLLC scheme under the specified operating conditions. However, experimental and hardware-in-the-loop (HIL) validation have not yet been conducted. Considering inverter switching processes, variations in grid impedance, and interactions between active control and passive resonant branches during practical operation, further evaluation of the scheme's compensation performance and stability under real operating conditions is required.

Author Contributions: F.Z.: conceptualization, writing—review and editing, supervision. S.Z. (Shuhang Zhang): writing—original draft preparation. S.L.: writing—original draft preparation. Y.S.: resources. C.Y.: resources. S.Z. (Shengqi Zhou): Resources. J.L.: methodology, validation. All authors have read and agreed to the published version of the manuscript.

Funding: This research received no external funding.

Data Availability Statement: The data that support the findings of this study are available from the corresponding author upon reasonable request.

Conflicts of Interest: Author Shun Li was employed by the company State Grid Shandong Electric Power Company Qingdao Huangdao District Power Supply Company. Author Yukun Su was employed by the company State Grid Shandong Province Electric Power Corporation Xintai Power Supply Company. Authors Chao Yang and Shengqi Zhou were employed by the company State Grid Shandong Electric Power Company Qingdao Power Supply Company. Author Jingui Lv was employed by the company Qingdao Hisense Hitachi Air-Conditioning Systems Co., Ltd. The remaining authors declare that the research was conducted in the absence of any commercial or financial relationships that could be construed as a potential conflict of interest.

Nomenclature

High-RE-PE	A High Proportion of Renewable Energy and A High Proportion of Power Electronics
APF	Active Power Filter
PV	Photovoltaic
PI	Proportional–Integral
quasi-PR	Quasi-Proportional Resonant
FFT	Fast Fourier Transform
THD	Total Harmonic Distortion
MPPT	Maximum Power Point Tracking

References

1. Etanya, T.F.; Tsafack, P.; Ngwashi, D.K. Grid-connected distributed renewable energy generation systems: Power quality issues, and mitigation techniques—A review. *Energy Rep.* **2025**, *13*, 3181–3203. [CrossRef]
2. Kaur, J.; Bath, S.K. Harmonic distortion in power systems due to electronic control and renewable energy integration: A comprehensive review. *Discov. Electron.* **2025**, *2*, 67. [CrossRef]
3. Yuan, W.Q.; Yuan, X.; Xu, L.W.; Zhang, C.; Ma, X.S. Harmonic Loss Analysis of Low-Voltage Distribution Network Integrated with Distributed Photovoltaic. *Sustainability* **2023**, *15*, 4334. [CrossRef]
4. Li, G.X.; Tang, G.F.; Liu, X. A Quasi-Harmonic Voltage Compensation Control of PV Grid-Connected Converter for Suppressing Sub/Super-Synchronous Oscillation in Weak Grid. *IEEE J. Emerg. Sel. Top. Power Electron.* **2024**, *12*, 4144–4153. [CrossRef]
5. Du, W.J.; Ma, Z.C.; Wang, Y.; Wang, H.F. Harmonic Oscillations in a Grid-Connected PV Generation Farm Caused by an Increased Number of Parallel-Connected PV Generating Units and Damping Controllers. *CSEE J. Power Energy Syst.* **2024**, *10*, 2350–2359.
6. Wang, C.; Wang, X.H.; He, Y.Y.; Pan, D.H.; Zhang, H.; Ruan, X.B.; Chen, X. Passivity-Oriented Impedance Shaping for LCL-Filtered Grid-Connected Inverters. *IEEE Trans. Ind. Electron.* **2023**, *70*, 9078–9090. [CrossRef]
7. Han, Z.J.; Yuan, S.; Zhang, J.N.; Zheng, X.; Dong, H. Analysis of harmonic characteristics and impact of microgrid. *Northeast Power Technol.* **2021**, *42*, 1–9. [CrossRef]
8. Zhe, H.; Yang, H.; Zalhaf, A.S.; Zhou, S.; Zhao, E.; Yang, P. Harmonic Sources Modeling and Characterization in Modern Power Systems: A Comprehensive Overview. *Electr. Power Syst. Res.* **2023**, *218*, 109234. [CrossRef]
9. Xu, S.; Tao, S.; Xu, Y. Secondary sideband harmonic emission characteristics of individual/multi-parallel grid-connected inverters. *Int. J. Electr. Power Energy Syst.* **2025**, *170*, 110816. [CrossRef]
10. Li, R.; Li, Y.; Li, J.; Bao, C.; Zhang, T. A damping-reuse-based inverter topology reconfiguration method for wideband resonance suppression. *IET Power Electron.* **2026**, *19*, e70202. [CrossRef]
11. Hossain, M.K.; Chowdhury, P.; Nowshin, I.; Islam, M.R.; Al-Hysam, A.; Farrok, O. Grid-connected inverter for photovoltaic energy harvesting: Advances in topologies and control techniques. *Energy Convers. Manag. X* **2026**, *29*, 101422. [CrossRef]
12. Karimi, M.; Mokhlis, H.; Naidu, K.; Uddin, S.; Bakar, A.H.A. Photovoltaic Penetration Issues and Impacts in Distribution—A Review. *Renew. Sustain. Energy Rev.* **2016**, *53*, 594–605. [CrossRef]

13. Erenoğlu, K.; Çiçek, A.; Arıkan, O.; Erdinç, O.; Catalão, J.P.S. A new approach for grid-connected hybrid renewable energy system sizing considering harmonic contents of smart home appliances. *Appl. Sci.* **2019**, *9*, 3941. [CrossRef]
14. Zhao, E.S.; Han, Y.; Lin, X.Y.; Yang, P.; Blaabjerg, F.; Zalhaf, A.S. Impedance Characteristics Investigation and Oscillation Stability Analysis for Two-Stage PV Inverter under Weak Grid Condition. *Electr. Power Syst. Res.* **2022**, *209*, 108053. [CrossRef]
15. Shao, Z.G.; Xu, H.B.; Xiao, S.Y.; Wu, G.C.; Zhang, Y. Harmonic problems in new energy grids. *Power Syst. Prot. Control* **2021**, *49*, 178–187.
16. Herman, L.; Knez, K.; Blazic, B. Design and Performance Evaluation of a Hybrid Active Power Filter Controller. *Energies* **2024**, *17*, 2492. [CrossRef]
17. Karadeniz, A.; Balci, M.E.; Abdel Aleem, S.H.E. Cost-effective Optimal Hybrid Active Power Filter Design to Maximize Loading Capacity of Power Transformers in Harmonic-rich Systems. *Electr. Eng.* **2026**, *108*, 137. [CrossRef]
18. Zhao, Y.X.; Yin, M.Y.; Fan, H.; Mei, Q.M. Parameter Optimization Method of Photovoltaic Grid-Connected Inverter LCLLC Filter Based on Improved Multi-objective Particle Swarm Optimization Algorithm. *Water Resour. Power* **2024**, *42*, 213–217.
19. Jia, X.; Yu, S.; Zhang, Y.; Feng, Y.; Zhou, B. LCL grid-connected inverter resonance feedforward-active damping hybrid control strategy for mitigating weak grid resonance and harmonic currents. *Energies* **2025**, *18*, 6010. [CrossRef]
20. Cheepati, K.R.; Parimalasundar, E.; Suresh, K.; Reddy, C.R.; Alqahtani, M.M.; Khalid, M. Design of Triple Tuned Passive Harmonic Power Filter-A Novel Approach. *IEEE Can. J. Electr. Comput. Eng.* **2023**, *46*, 269–277. [CrossRef]
21. Liu, X.Y.; Ma, H.K. Quasi-proportional Resonance Control Strategy Based on Hybrid Active Power Filter. *Comput. Simul.* **2024**, *41*, 123–128.
22. Ding, H.F.; Wang, J.C.; An, C.C.; Fei, J.T. Chebyshev Petri recursive fuzzy neural sliding mode control for active power filter. *Eng. Appl. Artif. Intell.* **2026**, *17*, 114578. [CrossRef]
23. Daou, N.; Chabani, M.S.; Achour, B.; Zouzou, S.E.; Pu, V.; Mossa, M.A.; Almalki, M.M. Robust second-order sliding-mode backstepping control of the parallel active filter for harmonics and reactive power compensation-experimental validation. *Energy Rep.* **2026**, *15*, 109117. [CrossRef]
24. Das, S.R.; Ray, P.K.; Sahoo, A.K.; Ramasubbareddy, S.; Babu, T.S.; Kumar, N.M.; Elavarasan, R.M.; Mihet-Popa, L. A Comprehensive Survey on Different Control Strategies and Applications of Active Power Filters for Power Quality Improvement. *Energies* **2021**, *14*, 4589. [CrossRef]
25. Ray, P.; Senapati, L.; Behera, P.K.; Mohapatra, A.; Kambo, T.A.T.; Samantaray, S.; Sahoo, B. Adaptive control of a PV-integrated unified power quality conditioner for remote low-voltage distribution networks. *IET Renew. Power Gener.* **2026**, *20*, e70280. [CrossRef]
26. Agrawal, N.; Singh, S.K.; Agarwal, A.; Kanumuri, T.; Singh, S.N. A dual-mode solar PV-integrated shunt active power filter with reduced-switch count for grid support and power quality enhancement in hybrid energy systems. *Electr. Power Syst. Res.* **2026**, *256*, 112907. [CrossRef]
27. Sou, W.K.; Chao, C.W.; Gong, C.; Lam, C.S.; Wong, C.K. Analysis, Design, and Implementation of Multi-Quasi-Proportional-Resonant Controller for Thyristor-Controlled LC-Coupling Hybrid Active Power Filter (TCLC-HAPF). *IEEE Trans. Ind. Electron.* **2022**, *69*, 29–40. [CrossRef]
28. Nafack Nihako, J.; Simo, E.; Abada Essouma, D.D.; Leutchouang, M.N.; Tsakem, C.R.A.; Tchienou, C.Y.T.; Watia, J.S.K.; Logerais, P.; Djouda, J.M. Realistic Modeling of Photovoltaic Solar Cell: A Simple and Accurate Two-Diode Model. *Appl. Res.* **2025**, *4*, e70010. [CrossRef]
29. Lo Brano, V. Open and reproducible estimation of PV single-diode parameters from datasheet data. *Energy Rep.* **2026**, *15*, 109280. [CrossRef]
30. Liu, E.J.; Huang, Y.H.; Lin, W.L.; Wen, C.-K.; Lin, C.-I. Rapid, precise parameter optimization and performance prediction for multi-diode photovoltaic model using Puma Optimizer. *Energies* **2025**, *18*, 2855. [CrossRef]
31. Shen, X.; Wu, Y.; Yuan, Q.; He, J.; Zhou, C.; Shen, J. Characteristic study of a typical satellite solar panel under mechanical vibrations. *Micromachines* **2024**, *15*, 996. [CrossRef]
32. Sun, M.; Jiang, H.B. Analysis of output characteristics of grid-connected photovoltaic inverter and modeling of harmonic sources. *Electr. Autom.* **2020**, *42*, 71–74.
33. Riba, J.R. The Role of AC Resistance of Bare Stranded Conductors for Developing Dynamic Line Rating Approaches. *Appl. Sci.* **2024**, *14*, 8982. [CrossRef]
34. Mariscotti, A.; Mingotti, A. The Effects of Supraharmonic Distortion in MV and LV AC Grids. *Sensors* **2024**, *24*, 2465. [CrossRef]
35. Zhang, B.; Liu, Y.; Zhao, K. Transformer loss calculation and analysis driven by load harmonic. In Proceedings of the International Conference on Electrical and Control Engineering, Yichang, China, 16–18 September 2011; pp. 1394–1398.
36. León-Martínez, V.; Peñalvo-López, E.; Montañana-Romeu, J.; Andrada-Monrós, C.; Molina-Cañamero, L. Assessment of Load Losses Caused by Harmonic Currents in Distribution Transformers Using the Transformer Loss Calculator Software. *Environments* **2023**, *10*, 177. [CrossRef]

37. León-Martínez, V.; Peñalvo-López, E.; Sáiz-Jiménez, J.Á.; León-Vinet, A. Revisited Concept of Three-Phase Transformers' Short-Circuit Resistances in Light of the IEEE Standard C57.110-2018. *Appl. Sci.* **2024**, *14*, 3126. [CrossRef]
38. Wei, C.F.; Li, Q.L.; Jiang, J.D. Quantitative calculation and modeling simulation of distribution network losses taking into account harmonic factors. *J. Zhengzhou Univ. Eng. Ed.* **2018**, *39*, 53–66.
39. *C57.110-2018*; IEEE Recommended Practice for Establishing Liquid-Immersed and Dry-Type Power and Distribution Transformer Capability When Supplying Nonsinusoidal Load Currents. IEEE: Piscataway, NJ, USA, 2018.
40. Miteva, N.; Sima, L.; Dagan, K.J. Power loss calculation in oil-type distribution transformers supplying nonlinear loads. *Electronics* **2025**, *14*, 2500. [CrossRef]
41. Zhou, Q.; Dian, Y.; Liu, X.; Leng, M.; Chen, C.; Liu, H. Measurement and Assessment of Reactive, Unbalanced and Harmonic Line Losses. *Electronics* **2024**, *13*, 1680. [CrossRef]
42. Ikić, M.; Mikulović, J. Experimental evaluation of distortion effect for grid-connected PV systems with reference to different types of electric power quantities. *Energies* **2022**, *15*, 416. [CrossRef]
43. Klaić, Z.; Knežević, G.; Primorac, M.; Topić, D. Impact of photovoltaic and biogas power plant on harmonics in distribution network. *IET Renew. Power Gener.* **2020**, *14*, 110–117. [CrossRef]
44. Zhong, C.; Wang, P.; Liu, C.; Guo, D.; Wang, R.; Liu, Y. Optimal harmonic compensation for grid-connected photovoltaic inverters under limited compensation margin. *Electr. Power Syst. Res.* **2025**, *241*, 111406. [CrossRef]
45. Gaiceanu, M.; Marin, G.A.; Epure, S.; Buhosu, R.; Vlad, C. Integrated hierarchical control architecture with adaptive state–parameter estimation for a three-phase shunt active power filter. *Energies* **2026**, *19*, 4546. [CrossRef]
46. Wu, Z.; Xu, G.; Zhu, W.; Sheng, G. A dispersing proportional resonance controller for selective harmonic current compensation in a shunt active power filter. *IEEE Trans. Power Electron.* **2025**, *40*, 279–289. [CrossRef]
47. Zeng, M.; Li, G.M.; Yan, Y.; Li, J.F.; Dong, J. Grid-connected current optimization of LCL-type single-phase PV with DC feedforward based on quasi-PR and PI composite control. *J. Nat. Sci. Hunan Norm. Univ.* **2020**, *43*, 80–86.
48. Wang, X.Y.; Mao, R.P.; Tian, B.Y.; Huang, J. Grid-connected PV current optimization based on joint PI and quasi-PR control. *Power Syst. Prot. Control* **2017**, *45*, 121–125.
49. *GB 51204-2016*; Technical Code for Electromagnetic Compatibility of Electrical Engineering of Building. China Planning Press: Beijing, China, 2017.
50. Refaie Ali, A.; Islam, M.R.; Islam, S.; Zohura, F.T.; Nurhidayat, I. Design a passive filter in combination with SAPF to improve the power quality of the solar hybrid micro-grid system and combustion engines. *Sustain. Energy Res.* **2025**, *12*, 52. [CrossRef]

Disclaimer/Publisher's Note: The statements, opinions and data contained in all publications are solely those of the individual author(s) and contributor(s) and not of MDPI and/or the editor(s). MDPI and/or the editor(s) disclaim responsibility for any injury to people or property resulting from any ideas, methods, instructions or products referred to in the content.